



**HAL**  
open science

## Characterizing spray flame–vortex interaction: A spray spectral diagram for extinction

Benedetta Franzelli, Aymeric Vié, Matthias Ihme

### ► To cite this version:

Benedetta Franzelli, Aymeric Vié, Matthias Ihme. Characterizing spray flame–vortex interaction: A spray spectral diagram for extinction. *Combustion and Flame*, 2016, 163, 10.1016/j.combustflame.2015.09.006 . hal-01272955

**HAL Id: hal-01272955**

**<https://hal.science/hal-01272955>**

Submitted on 13 Mar 2017

**HAL** is a multi-disciplinary open access archive for the deposit and dissemination of scientific research documents, whether they are published or not. The documents may come from teaching and research institutions in France or abroad, or from public or private research centers.

L'archive ouverte pluridisciplinaire **HAL**, est destinée au dépôt et à la diffusion de documents scientifiques de niveau recherche, publiés ou non, émanant des établissements d'enseignement et de recherche français ou étrangers, des laboratoires publics ou privés.

# Characterizing spray flame-vortex interaction: a spray spectral diagram for extinction

Benedetta Franzelli<sup>a,b</sup>, Aymeric Vié<sup>\*\*a</sup>, Matthias Ihme<sup>\*a</sup>

<sup>a</sup>Center for Turbulence Research, Stanford University, Stanford, CA 94305, USA

<sup>b</sup>Laboratoire EM2C, CNRS, CentraleSupelec, Grande Voie des Vignes, 92295 Chatenay-Malabry, France

---

## Abstract

The flame-vortex interaction is a preferred configuration for the understanding of flame-turbulence interaction as well as for the development of turbulent combustion models. This configuration has been extensively studied in the literature for gaseous flames. In the present work, we extend this analysis, and develop a spectral diagram for the description of spray flame-vortex interaction in analogy to purely gaseous flames in the limit of momentum equilibrium. The focus is hereby on the analysis of competing time-scale effects that are associated with droplet evaporation, mixing and reaction chemistry. Through this analysis, a new extinction scenario is identified that is specific to spray flames as a result of fuel depletion. The derived spectral diagram is confirmed by numerical investigations for n-dodecane counterflow spray flames interacting with a pair of vortices. The different extinction scenarios as well as their dependence on the evaporation time are numerically studied and verified.

*Key words:* Spray flame-vortex interaction; Spectral diagram; Extinction

---

## Contents

<b>1</b>	<b>Introduction</b>	<b>2</b>
<b>2</b>	<b>Spectral diagram for spray flame-vortex interaction</b>	<b>3</b>
2.1	Background: Gaseous flame-vortex interaction . . . . .	3
2.2	Spray flame characterization and assumptions . . . . .	4
2.3	Spray spectral diagram . . . . .	6
<b>3</b>	<b>Detailed simulations of spray-flame-vortex interaction</b>	<b>8</b>
3.1	Gas-phase and dispersed-phase equations . . . . .	9
3.2	Reaction chemistry . . . . .	10
3.3	Numerics . . . . .	10
3.4	Configuration . . . . .	10
<b>4</b>	<b>Results and discussion</b>	<b>11</b>
4.1	Structure of steady gaseous and spray flames . . . . .	11
4.2	Examples of spray flame-vortex interaction . . . . .	11
4.3	Effect of Lefebvre number . . . . .	18

---

\*Corresponding author

\*\*Now at Laboratoire EM2C, CNRS, CentraleSupelec.

*Email addresses:* [benedetta.franzelli@cnrs.fr](mailto:benedetta.franzelli@cnrs.fr) (Benedetta Franzelli), [aymeric.vie@ecp.fr](mailto:aymeric.vie@ecp.fr) (Aymeric Vié), [mihme@stanford.edu](mailto:mihme@stanford.edu) (Matthias Ihme)

<b>5</b>	<b>Conclusions</b>	<b>20</b>
	<b>References</b>	<b>21</b>
	<b>Nomenclature</b>	<b>22</b>
<b>A</b>	<b>Effect of the vortex injection side on flame-vortex interaction</b>	<b>25</b>
<b>B</b>	<b>A-priori evaluation of the reference evaporation time scale</b>	<b>25</b>
<b>C</b>	<b>Effect of boundary conditions: pre-vaporized case</b>	<b>26</b>

## 1. Introduction

The fundamental understanding of turbulence-flame interaction is of relevance for practical applications, since turbulence may drastically modify the combustion process by affecting the flame structure, thus possibly impacting pollutant emissions, thermo-acoustic instabilities, local quenching and reignition [1]. With regard to application to Large-Eddy Simulation (LES) and Reynolds-Average Navier-Stokes (RANS) modeling, it is therefore required to accurately model the interaction between the flow field and the flame on the computationally unresolved scales.

In the context of gaseous flames, several studies have been performed to investigate the complex interaction of a vortex with premixed [2, 3, 4] and non-premixed flames [5, 6, 7] to mimic the turbulence effect on combustion. In particular, a flamelet regime was identified, in which the turbulent flame front is seen as a collection of one-dimensional flames that are stretched and deformed by vortices [5].

Under this assumption, the understanding of flame-vortex interaction is essential for numerous practical combustion applications [1]. The interaction of a pair of vortices with a laminar flame represents a canonical configuration for the theoretical understanding of combustion mechanisms in turbulent flows [8] and the development and validation of turbulent combustion models [9]. Indeed, the effect of a pair of vortices on a laminar flame can be studied to examine several combustion regimes that are representative for turbulent flows [8]. For purely gaseous flames, such an idealized configuration has led to several studies, either in premixed and non-premixed regimes, see [1] for an exhaustive overview. In addition, findings from these studies have led to the construction of combustion spectral diagrams [4, 10, 11, 12] that are of particular importance for the derivation of new combustion models for turbulent flow applications.

In the context of spray flames, less efforts have been made towards the understanding of combustion regimes. In [13], the investigation of a 3D swirled spray flame through Direct Numerical Simulation (DNS) has shown the complexity of spray flames, in which premixed, partially premixed and diffusion reaction zones may coexist. In [14], the authors studied the interaction of a counterflow spray flame with turbulence, confirming the existence of a flamelet regime for spray flames. As such, the study of a spray flame interacting with a pair of vortices may provide a fundamental understanding of the competition between evaporation, mixing and combustion for a range of practically relevant operating regimes. Although flame-vortex interaction is recognized as a canonical configuration for examining the coupling between combustion and turbulence in gaseous configurations, the investigation of spray flames in these configurations has been limited to phenomenological observations [15, 16, 17, 18] and asymptotic analysis [19].

The objective of this work is to extend the knowledge of spray flame-vortex interaction by combining theoretical and numerical ~~analyse~~ analyse. In particular, the interaction of a pair of vortices with a spray flame in the limit of zero slip velocity is considered in order to identify the effect of evaporation on combustion regimes for turbulent spray flames. Particular attention is attributed to the investigation of local extinction. A new combustion diagram that is generalized to spray flames is here analytically derived by following the work of Vera et al. [11] for purely gaseous flames. This regime diagram is subsequently verified through detailed numerical simulations.

The remainder of this paper is organized as follows. We first present in Section 2 the theoretical derivation of the new spectral diagram for spray flame-vortex interaction, following the rationale of [11]. The modeling

approach that is used for the computational verification and the computational approach are presented in Section 3. Numerical results are presented in Section 4, first examining the steady state structure of the counterflow flame. Examples of possible scenarios of spray flame-vortex interaction are analyzed to highlight different responses of a spray flame to the vortex passage compared to the corresponding gaseous flame. To verify the theoretically developed spectral diagram, the role of the evaporation time is finally characterized. The paper finishes with conclusions.

## 2. Spectral diagram for spray flame-vortex interaction

### 2.1. Background: Gaseous flame-vortex interaction

The flame-vortex interaction is a canonical configuration for examining basic phenomena that control the coupling between combustion and turbulence. By considering this configuration, Renard et al. [1] developed a fundamental understanding of different combustion modes that are summarized in a so-called “spectral diagram”. With relevance to the present work, we briefly summarize the classical results for gaseous flames.

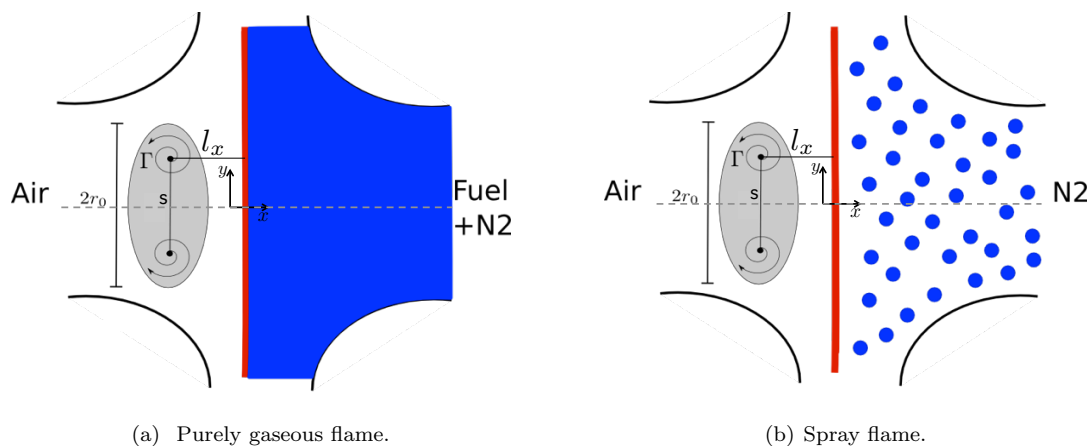


Figure 1: Schematic of the flame-vortex interaction for (a) purely gaseous flame and (b) spray flame: two counter-rotating vortices are superimposed to the initial steady-state solution of the counterflow flame. (For interpretation of the references to colour in this figure, the reader is referred to the web version of this article.)

The configuration consists of a strained non-premixed flame, in which a nitrogen-diluted fuel mixture is injected against an oxidizer stream (see Fig. 1(a)). The flame has a characteristic flame-front speed  $S_L \sim D_{th}/\delta_L$ , where  $D_{th}$  is the thermal diffusivity,  $\delta_L$  is flame-front thickness and the chemical time scale is  $\tau_c \sim D_{th}/S_L^2$ . Due to the unperturbed flow, the flame is subjected to a global strain rate  $A_0$ . The steady gaseous flame is governed by the competition of mixing, advecting and chemical processes. Two non-dimensional numbers are then sufficient to characterize the flame: the Peclet number  $Pe = A_0 L^2/D_{th}$  (with  $L$  a characteristic length), describing the ratio between mixing and advection contribution, and the Damköhler number:

$$Da = \frac{\tau_{strain}}{\tau_c} = \frac{1}{\tau_c A_0} \quad (1)$$

accounting for the competition between characteristic advection and chemical time scales.

In the flame-vortex configuration, a vortex ring of radius  $r_0$ , strength  $\Gamma$  and characteristic speed  $u_T \sim \Gamma/r_0$  is injected at the oxidizer side to interact with the flame front. As a result of the vortex interaction, the flame will experience a strain  $A_\Gamma = \Gamma/(2r_0^2)$ , and the flame can locally extinguish when  $A_\Gamma$  exceeds the critical extinction strain rate  $A_e$ .

In the following, the non dimension vortex strenght  $\tilde{\Gamma} = A_\Gamma/A_0$  is introduced to describe the flame-vortex interaction. The robustness of the flame  $R = A_e/A_0 \sim 1/(A_0 \tau_c) \sim Da^{-1}$  is also introduced. The Peclet

number is given by  $Pe = Pe_0 = A_0 r_0^2 / D_{th}$ . With this, different regimes can be identified by considering these three non-dimensional parameters ( $R$ ,  $Pe_0$  and  $\tilde{\Gamma}$ ) [11, 12]:

- Vortex dissipation: for small vortex strength, the vortex dissipates before reaching the flame front without affecting the flame. Consequently, no flame-vortex interaction occurs for:

$$\frac{\Gamma}{\nu} \leq 1 \Rightarrow Re_\Gamma \sim \tilde{\Gamma} Pe_0 \leq 1, \quad (2)$$

where  $Re_\Gamma = \Gamma/\nu$  is the Reynolds number based on the vortex strength.

- Thickened reaction zone: under the condition that the vortex is small compared to the flame thickness, the vortex penetrates the preheat flame region and enhances the mixing of the reactants. This results in a thickening of the preheat zone, but the inner flame structure is not affected by the vortex for:

$$\frac{r_0}{\delta_L} \leq 1 \Rightarrow r_0 \frac{S_L}{D_{th}} \sim (Pe_0 R)^{1/2} \leq 1. \quad (3)$$

- Local flame quenching: under the condition that the flame strength  $R$  is smaller than the non-dimensionalized vortex strength  $\tilde{\Gamma}$ , the flame is locally extinguished by the vortex pair:

$$\frac{A_e}{A_\Gamma} \leq 1 \Rightarrow Da_\Gamma^e = \frac{R}{\tilde{\Gamma}} \leq 1, \quad (4)$$

where  $Da_\Gamma^e = A_e/A_\Gamma$  is the Damköhler number at extinction.

- Flame re-ignition via edge flame: for the case of local extinction, the flame may re-ignite if the front propagation velocity<sup>1</sup>  $U_F$  is of the same order as the flow velocity  $A_0 r_0$  [11]:

$$U_F \geq A_0 r_0 \Rightarrow (Pe_0 R^{-1})^{1/2} < f_\infty \quad (5)$$

with  $f_\infty \approx 3$  [20, 21].

Turbulent vortices and unsteady chemistry effects could also be taken into account [11], introducing additional regions in the spectral diagram.

## 2.2. Spray flame characterization and assumptions

Compared to a purely gaseous flame, the spray has a compounding effect on the flame due to the introduction of additional characteristic time scales, namely the evaporation time  $\tau_v$  and the droplet drag time  $\tau_p$ . In this asymptotic analysis, the following assumptions are considered:

- Both  $\tau_v$  and  $\tau_p$  are assumed to be constant. A relation for this time scale ratio can be written as [22]:

$$\frac{\tau_p}{\tau_v} = \frac{4 \ln(1 + B_M)}{9 Sc} = \frac{St_p}{St_v}, \quad (6)$$

where  $B_M$  is the Spalding number,  $Sc$  is the Schmidt number of the gas phase,  $St_p = \tau_p A_0$  is the drag Stokes number, and  $St_v = \tau_v A_0$  is the evaporation Stokes number. These two additional characteristic time scales affect the flow-field quantities and the flame characteristics, compared to the corresponding gaseous flame.

- One-way coupling is considered to examine the effect of the evaporation time. This assumption is reasonable when considering that the droplets follow the mean flow:  $St_p = \tau_p A_0 \ll 1 \Rightarrow St_p/St_v \ll (A_0 \tau_v)^{-1}$ .

<sup>1</sup>Note that the velocity  $U_F$  is not equal to the laminar flame speed  $S_L$ , as it is well recognized for triple flames [12].

- Gas and spray phases are assumed at momentum equilibrium, i.e there is no slip velocity between both phases [23]. This assumption allows to isolate the vaporization part of the spray physics, since the contribution of the drag force is zero. This is a reasonable assumption in the limit  $St_p \rightarrow 0$ .
- The main contribution of the evaporation time is the change of the characteristic quenching time  $\tau_q$  of the flame, as suggested by Ballal and Lefebvre [24]:

$$\tau_q = \tau_v + \tau_c, \quad (7)$$

This assumption implicitly assumes that the two phenomena occur sequentially and do not spatially overlap.

By introducing these assumptions, the problem is simplified to isolate the role of the evaporation time on the spray flame-vortex interaction. As such, the asymptotic analysis proposed in the following is strictly valid in the limit of zero slip velocity, but it is expected to provide a reasonable estimation of flame-vortex interaction for  $St_p < 0.25$ , when no droplet stagnation plane crossing occurs. Under such assumptions, the relation between the flame speed and the flame time is extended to spray flames such as:  $S_L^\diamond \approx \sqrt{D_{th}/\tau_q}$ , and other flame properties can be derived from the gaseous flame values:

$$\frac{S_L}{S_L^\diamond} \sim \sqrt{\frac{\tau_q}{\tau_c}} = \sqrt{1 + \frac{\tau_v}{\tau_c}}, \quad (8a)$$

$$\frac{Da_\Gamma^e}{Da_\Gamma^{e,\diamond}} \sim \frac{A_e}{A_e^\diamond} \sim \frac{\tau_q}{\tau_c}, \quad (8b)$$

where the superscript  $\diamond$  denotes the spray flame quantities. The characterization of a steady non-premixed spray flame requires the introduction of an additional non-dimensional number accounting for the presence of the evaporation process, competing with the other phenomena. The evaporation Stokes number  $St_v$  can be considered. Alternatively, a more appropriate non-dimensional number, namely the Lefebvre number, is introduced here to account for the competition between evaporation and chemical times:

$$Lf = \frac{\tau_v}{\tau_c} = St_v Da. \quad (9)$$

For small values of  $Lf$ , the evaporation time is small compared to the chemical time so that quenching is mainly governed by chemistry and the flame properties are only slightly modified by evaporation. Indeed, for  $Lf \ll 1$ , a pre-evaporating flame is retrieved, whereas a purely gaseous flame is characterized by  $Lf = 0$ . In contrast, for larger values of  $Lf$  the evaporation process is expected to largely modify the flame properties and, consequently, the flame-vortex interaction. For  $Lf \gg 1$ , the vaporization process is too long compared to  $\tau_c$ , so that the gaseous fuel provided by evaporation may not be sufficient to sustain combustion.

From Eq. 8, the Lefebvre number allows to describe the effect of the evaporation time on the flame characteristics, compared to the corresponding purely gaseous flame:

$$S_L^\diamond \sim (1 + Lf)^{-1/2} S_L, \quad (10a)$$

$$Da_\Gamma^{e,\diamond} \sim (1 + Lf)^{-1} Da_\Gamma^e. \quad (10b)$$

The flame-front thickness, which depends only on the chemical time  $\tau_c$ , is unchanged for spray flames and equal to  $\delta_L$ . These relations are supported by experimental and numerical data for stoichiometric premixed spray flames [24, 25] and the simulation presented in Section 4. Equation (8b) shows that the modified Damköhler number at the extinction strain rate reduces for large values of the  $Lf$  number, implying that a spray flame extinguishes for smaller strain rates compared to a gaseous flame as found in [26]. In [27], the front propagation velocity  $U_F$  for purely gaseous flames is observed to be a function of the Damköhler

number, which presents an asymptotic value. This behavior is here also assumed for spray flames:

$$\frac{U_F}{S_L} \frac{1}{f_\infty} = f(\text{Da}/\text{Da}^e) \sim 1 \Rightarrow \frac{U_F^\diamond}{S_L^\diamond} \frac{1}{f_\infty^\diamond} = f(\text{Da}^\diamond/\text{Da}^{e,\diamond}) \sim 1. \quad (11)$$

where  $\text{Da}^e$  is the local Damköhler number at extinction as defined in [27].

### 2.3. Spray spectral diagram

The spectral diagram is here extended to consider the interaction of a pair of vortices with a spray flame.

In the spray flame-vortex configuration, the fuel spray is injected together with gaseous nitrogen against a stream of oxidizer. In analogy with the classical analysis for gaseous flames the following assumptions are invoked:

- the vortex is injected only from the oxidizer side. This choice has been considered for most studies on flame-vortex interactions [10, 28]. The effect of the vortex injection at the fuel side has been experimentally observed by Santoro et al. [15] and is here numerically examined in Appendix A.
- Equal diffusivities for all species is considered to avoid differential diffusion effects on the flame-vortex interaction [29]. This is a broadly-used assumption and its impact has been discussed in [29].

The configuration under investigation is schematically presented in Fig. 1(b), and essential features that characterize flame/vortex interactions are shown in Fig. 2 [30]. Once the vortex pair reaches the flame front (colored in red in Fig. 2(a)), it interacts with the flame structure, which may be locally modified by the induced stretch. For sufficiently high vortex strength, the flame is engulfed by vortices, creating a dome in the flame. In this case, the maximum induced strain rate is located at the top hat region, whereas curvature effects dominate in the hat brim (see Fig. 2(a)). In the case of a spray flame, the droplets are subjected to centrifugal forces of the vortex. The modification of the flame reaction zone as well as the preferential droplet concentration due to the vortex passage affect the evaporation process and flame position (shown in blue in Fig. 2(b)). With this, the classical asymptotic analysis, discussed in [31] for gaseous flame/vortex

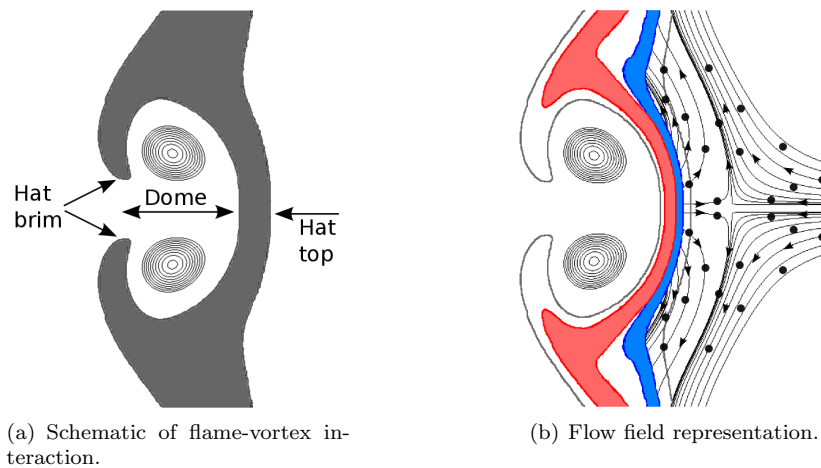


Figure 2: Qualitative features of a flame-vortex interaction [30]. The grey, red and blue regions in (b) identify the diffusion layer, the inner reaction zone and the evaporation zone, respectively. Streamlines are added to illustrate the droplet trajectories. (For interpretation of the references to colour in this figure, the reader is referred to the web version of this article.)

interaction, is extended to spray flames using expressions (10) and (11) to relate gaseous and spray flame properties. Compared to the regime diagram for gaseous flames, an additional third dimension, accounting for the ratio between evaporation and chemical time scales expressed by the  $L_f$  number, has to be considered. By considering only the effect of the evaporation time on the criteria given in Section 2.1, it is possible to

define the limits of the spectral diagram for spray flame-vortex interactions, presented in Fig. 3. The flame-vortex interaction is here represented as a function of the characteristic speed  $u_T \sim \Gamma/r_0$  and size  $l_T \sim r_0$  of the vortex, which are normalized by the characteristic flame-front velocity  $S_L$  and thickness  $\delta_L$ , respectively. By considering the four non-dimensional parameters  $(R, Pe_0, \tilde{\Gamma}, Lf)$ , the following regimes can be distinguished:

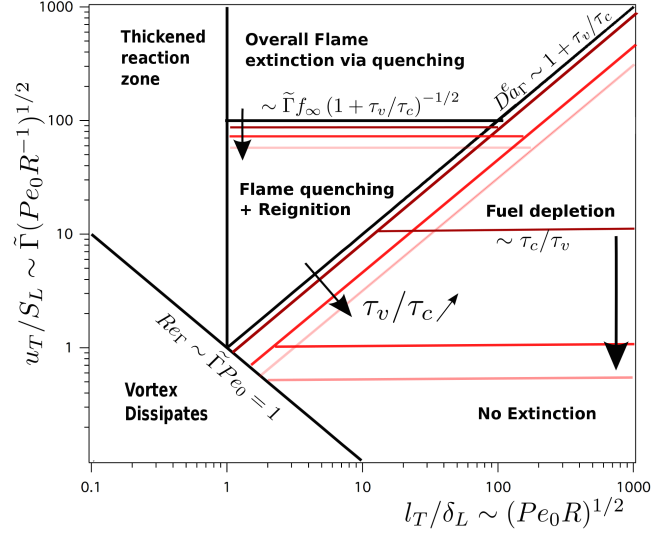


Figure 3: Spectral diagram for spray flame-vortex interaction. Black lines limit the different combustion regimes that were found analytically for gaseous flames [11, 12]. Red lines correspond to spray flames with increasingly higher evaporation time. (For interpretation of the references to colour in this figure, the reader is referred to the web version of this article.)

- The vortex dissipation region ( $Re_\Gamma \leq 1$ ) is constrained by a diagonal line with a logarithmic slope of  $n = -1$  in the spectral diagram:

$$\frac{u_T}{S_L} \frac{l_T}{\delta_L} \sim \tilde{\Gamma} Pe_0 \leq 1. \quad (12)$$

This area is identical with that for purely gaseous combustion since the spray is assumed to not affect the flow-field and vortex properties.

- The thickened reaction zone ( $l_T/\delta_L \sim 1$ ) is identified by a vertical line in the spectral diagram:

$$\frac{l_T}{\delta_L} \sim (R Pe_0)^{1/2} \leq 1. \quad (13)$$

Since the size of the inner reaction zone is not affected by the evaporation time, this region is identical to that of gaseous flames.

- The local flame quenching region ( $Da_\Gamma^{e,\circ} \leq 1$ ) is represented by a diagonal in the spectral diagram:

$$\frac{u_T}{S_L} \frac{\delta_L}{l_T} \sim \frac{1}{Da_\Gamma^e} \sim \tilde{\Gamma} R^{-1} \leq (1 + Lf)^{-1}. \quad (14)$$

This relation shows that the extinction area increases for larger values of  $Lf$  implying that for spray flames local extinction occurs for smaller values of the strain rate induced by the vortex compared to the corresponding gaseous flame.

- The reignition condition ( $U_F^\circ/S_L^\circ \leq f_\infty^\circ$ ) is valid for the region identified by a horizontal line in the  $u_T/S_L$ - $l_T/\delta_L$  diagram:

$$\frac{u_T}{S_L} \sim \tilde{\Gamma}(\text{Pe}_0 \text{R}^{-1})^{1/2} \leq \tilde{\Gamma} f_\infty^\circ \left( \frac{\text{Da}_\Gamma^{e,\circ}}{\text{Da}_\Gamma^e} \right)^{1/2} \leq \tilde{\Gamma} f_\infty^\circ (1 + \text{Lf})^{-1/2}. \quad (15)$$

The reignition area decreases with increasing Lf-number, showing that for large droplet diameters, i.e. large  $\tau_v$  values, the flame is more likely to globally extinguish than for the corresponding purely gaseous flame, characterized by the same  $\tau_c$ . The value for  $f_\infty^\circ$  may be assumed to be of order of unity, in analogy to gaseous flames.

- The extinction of spray flames may also occur due to fuel depletion. This represents a new extinction mode that is not present in gaseous flames. At this condition, the competition between evaporation, mixing and advection is changed as vortices reach the flame. Under the assumption of negligible particle drag, i.e.  $\text{St}_p \ll 0.25$ , the droplets reach the stagnation point but they cannot pass through it [32]. As schematically presented in Fig. 2(b), close to the hat top the presence of the vortices inverts the velocity of the droplets which are pushed away from the flame front. As a consequence, fewer droplets are available for evaporation, resulting in a local fuel depletion. This in turn weakens the flame strength and enhances the extinction propensity. Flame extinction due to fuel depletion is expected to occur when the evaporating droplets, located next to the flame front, do not evaporate completely before exiting the flame reaction zone. This situation occurs when the thickness of the evaporation layer  $\delta_v \sim \tau_v u_T$  is smaller than the reaction layer:  $\delta_v < \delta_L$ . Under this condition, extinction by fuel depletion occurs:

$$\delta_v < \delta_L \Rightarrow \frac{u_T}{S_L} \sim \tilde{\Gamma}(\text{Pe}_0 \text{R}^{-1})^{1/2} \leq \text{Lf}^{-1}, \quad (16)$$

Criterion (16) compares the characteristic time of evaporation and mixing and is identified by a horizontal line in the spectral diagram, whose ordinate is given by the inverse of Lf. Therefore, this extinction region increases for flames characterized by the same chemical time  $\tau_c$  with increasing droplet diameter. This criterion is consistent with purely gaseous flames, for which  $\text{Lf}^{-1} \rightarrow \infty$ .

The effect of the competition between evaporation and combustion, represented by the Lefebvre number, on the spray-flame-vortex interaction is identified in Fig. 3. Here, the black lines limit the different interaction modes that were analytically found for gaseous flames whereas the red lines correspond to spray flames with increasingly higher Lf, which changes the way the vortex interacts with the flame by changing the characteristic flame properties.

In the following, this spectral diagram is verified through numerical simulations. It is noted that a complete characterization of the reignition phenomenon will require an extensive study on edge spray flames, in analogy with the work of Hermanns et al. [27] for gaseous flames. This, however, is beyond the scope of this study. Therefore, we will focus on the extinction phenomena without investigating the reignition stage through our simulations.

### 3. Detailed simulations of spray-flame-vortex interaction

In this section, detailed simulations are performed to computationally confirm the spectral diagram that was developed in the previous section.

### 3.1. Gas-phase and dispersed-phase equations

The gas phase is described by the conservation equations for mass, momentum, species, and energy:

$$\frac{\partial \rho}{\partial t} + \frac{\partial \rho u_j}{\partial x_j} = \dot{S}_m, \quad (17a)$$

$$\frac{\partial \rho u_i}{\partial t} + \frac{\partial \rho u_i u_j}{\partial x_j} = -\frac{\partial p}{\partial x_i} + \frac{\partial \sigma_{ij}}{\partial x_j} + \dot{S}_{u_i}, \quad (17b)$$

$$\frac{\partial \rho Y_k}{\partial t} + \frac{\partial \rho Y_k u_j}{\partial x_j} = \frac{\partial}{\partial x_j} \left( \rho D_k \frac{W_k}{W} \frac{\partial X_k}{\partial x_j} \right) + \dot{\omega}_k + \dot{S}_m \delta_{kF}, \quad (17c)$$

$$\frac{\partial \rho T}{\partial t} + \frac{\partial \rho T u_j}{\partial x_j} = \frac{\partial}{\partial x_j} \left( \rho D_{th} \frac{\partial T}{\partial x_j} \right) + \frac{\rho D_{th}}{c_p^2} \frac{\partial T}{\partial x_j} \frac{\partial c_p}{\partial x_j} + \dot{\omega}_T + \dot{S}_T, \quad (17d)$$

where  $\rho$  is the gas density,  $u_i$  is the  $i^{th}$  component of the gas velocity vector,  $\dot{S}_m$ ,  $\dot{S}_{u_i}$ , and  $\dot{S}_T$  are the source terms due to droplet evaporation, drag force, and heat transfer, respectively. The mass fraction of species  $k$  is denoted by  $Y_k$ . The pressure is denoted by  $p$ , and  $\sigma_{ij} = \mu \left[ \frac{\partial u_j}{\partial x_i} + \frac{\partial u_i}{\partial x_j} - \frac{2}{3} \frac{\partial u_k}{\partial x_k} \delta_{ij} \right]$  is the viscous stress tensor. The molecular weight of species  $k$  is denoted by  $W_k$  and  $W$  is the mixture-averaged molecular weight. The diffusivity of species  $k$  is denoted by  $D_k$ ,  $\dot{\omega}_k$  is the net production rate of species  $k$ , and  $\delta_{kF}$  is the Kronecker function that is unity for fuel (denoted by the index  $F$ ) and zero for all other species. The temperature is denoted by  $T$ ,  $c_p$  is the heat capacity, and  $h_k$  is the total sensible and chemical enthalpy of species  $k$ . The heat release  $\dot{\omega}_T$  is given by  $\dot{\omega}_T = -c_p^{-1} \sum_{k=1}^{N_s} h_k \dot{\omega}_k$ , where  $N_s$  is the number of species considered.

For the dispersed phase, a Lagrangian point-particle approach is used [33]. The equations describing each droplet are written as:

$$\frac{d\mathbf{x}_{d,i}}{dt} = \mathbf{u}_{d,i}, \quad (18a)$$

$$\frac{d\mathbf{u}_{d,i}}{dt} = \frac{f_1}{\tau_p} [\mathbf{u}_i(\mathbf{x}_d) - \mathbf{u}_{d,i}], \quad (18b)$$

$$\frac{dT_d}{dt} = \frac{\text{Nu}}{3\text{Pr}} \frac{c_p}{c_l} \frac{f_2}{\tau_p} [T(\mathbf{x}_d) - T_d] + \frac{\dot{m}_d l_v}{m_d c_l}, \quad (18c)$$

$$\frac{dm_d}{dt} = -\frac{\text{Sh}}{3\text{Sc}} \frac{m_d}{\tau_p} \ln(1 + B_M), \quad (18d)$$

where  $\mathbf{x}_d$  is the position of the droplet,  $\mathbf{u}_d$  its velocity,  $T_d$  its temperature, and  $m_d$  its mass. The Nusselt number is described by Nu, Pr is the Prandtl number and Sh is the Sherwood number. The relaxation time of the droplet is  $\tau_p = \rho_l d^2 / 18\mu$ ,  $\rho_l$  is its density,  $d$  is its diameter,  $c_l$  is its heat capacity and  $l_v$  is the latent heat of vaporization. The drag coefficient is  $f_1$ , accounting for high Reynolds number effects, and  $f_2$  is a correction factor to consider effects of heat exchange on the evaporation [33].

The coupling terms to the gas phase are obtained by integrating the contributions from all droplets contained in the control volume  $\Delta V$  [34]:

$$\dot{S}_m = - \left\{ \frac{dm_d}{dt} \right\}, \quad (19)$$

$$\dot{S}_{u_i} = - \left\{ \frac{dm_d u_{d,i}}{dt} \right\}, \quad (20)$$

$$\dot{S}_T = - \left\{ \frac{1}{c_p} \left[ c_l m_d \frac{dT_d}{dt} + (c_p T_d + l_v) \frac{dm_d}{dt} \right] \right\}, \quad (21)$$

where  $\{\cdot\} \equiv \frac{1}{\Delta V} \sum_{d \in \Delta V} \cdot$ .

To be consistent with the assumptions used to develop the analytical spectral diagram, gas and spray phases are assumed at momentum equilibrium, i.e. there is no slip velocity between both phases, so that  $u_{d,i} = u_i$  [23]. The heat transfer from the liquid to the gas is also assumed to be equal to zero, i.e.  $\dot{S}_T = 0$ , which is a reasonable assumption when the ratio  $\frac{\alpha_l \rho_l c_l}{\rho c_p}$  is small, where  $\alpha_l$  is the liquid volume fraction.

### 3.2. Reaction chemistry

In the present study, a 24-species mechanism for n-dodecane is used [14], which is based on the JetSurF 1.0 mechanism [35], originally consisting of 123 species and 977 reactions. This reduced mechanism has been validated in auto-ignition and perfectly stirred reactors [14] and guarantees a correct description of the flame structure and its response to strain rate variations. Detailed thermodynamic and transport properties are considered. The species diffusivities are calculated assuming unity Lewis number.

### 3.3. Numerics

The governing equations are solved in the low-Mach number limit using the structured 3DA code [36, 37]. The scalar advection operators are discretized using a QUICK scheme, and a second-order central differencing scheme is used for the momentum and pressure equations. The discrete Poisson system is solved using the HYPRE library [38]. A staggered representation is used: the velocity is defined at the cell face, while the scalars and density are located at the cell center. A second-order Crank-Nicholson scheme is used for time integration. The chemical source terms are evaluated using the DVODE library [39], based on the use of adaptive time stepping to advance the system of ODEs.

### 3.4. Configuration

We consider a two-dimensional counterflow configuration<sup>2</sup>, consisting of two opposed slots. The direction  $x_1 = x$  is the injection direction, the direction  $x_2 = y$  is the outflow. The separation distance between the two injectors is  $L_x = 0.1$  m, and  $L_y = 0.075$  m is the vertical domain length. The mesh consists of  $1000 \times 740$  cells, resulting in approximately 30 grid points to describe the reaction zone of the diffusion flame (whose thickness is  $\delta_L \approx 3$  mm). At the fuel side, gaseous nitrogen is injected with a fuel spray composed of n-dodecane at ambient condition ( $T_d^F = T^F = 300$  K). Here and in the following the superscripts ‘‘F’’ and ‘‘O’’ refer to the fuel side and the oxidizer side, respectively. The injection velocity of the liquid phase is identical to that of the gas phase,  $u^F = u^O = u_d^F = 2.5$  m/s, corresponding to a theoretical global flame strain rate of  $A_0 = 50$  s<sup>-1</sup>. The liquid mass flow rate is 9 g/s, corresponding to a purely gaseous composition of  $Y_{N_2}^F = 0.68$  and  $Y_{C_{12}H_{26}}^F = 0.32$ . The use of nitrogen at the fuel injection guarantees a diffusion-like combustion mode. The initial droplet distribution at injection is randomly drawn over the entire slot, resulting in a statistically homogeneous distribution. A parcel method is used so that each numerical droplet statistically represents  $N_p$  physical droplets [34].

On the oxidizer side, pure air is injected at  $T^O = 800$  K. These operating conditions ensure a robust flame (due to the relatively high temperature of the oxidizer mixture) with the liquid phase mainly evaporating in the preheat zone of the flame (due to the low temperature at the fuel side), preventing pre-vaporization.

Three different injection droplet diameters ( $d_0 = 25, 50, 75$   $\mu\text{m}$ ) are considered, corresponding to three different evaporation times  $\tau_v \sim K d_0^2$  ( $\tau_v \approx 0.75, 3.0, 675$  ms, respectively), where  $K$  is the regression rate.<sup>3</sup> Both  $R$  and  $Pe_0$  numbers are then constant in the steady calculations, so that the effect of the  $Lf$  number on the flame characteristics can be examined ( $Lf = 0.075, 0.3, 0.675$ , respectively, where  $\tau_c \approx 1.0$  ms from a laminar premixed stoichiometric calculation [11]). To keep the number of numerical droplets that are injected comparable for all configurations, we use  $N_p = 40, 10, 5$  for  $d_0 = 25, 50, 75$   $\mu\text{m}$ , respectively. From Eq. (6), the drag Stokes numbers are evaluated as  $St_p \approx 0.0375, 0.15, 0.34$ , respectively, so that the assumption of zero drag Stokes number is reasonable for all calculations. In particular, a simple calculation of the trajectory of the droplet in a flow with constant strain rate leads to maximum velocity differences of 3, 10, 21%, respectively, with negligible velocity reversal for the larger Stokes number.

<sup>2</sup>The third dimension is homogeneous. Droplets are still considered as spheres, and closure laws for drag/evaporation are still 3D.

<sup>3</sup>The methodology that is used to estimate  $\tau_v \sim K d_0^2$  from the initial droplet diameter  $d_0$  and the regression rate  $K$  is described in Appendix B.

## 4. Results and discussion

### 4.1. Structure of steady gaseous and spray flames

A direct comparison of the flame structure of the steady purely gaseous flame ( $Lf = 0$ ) and the spray flame for  $Lf = 0.3$  is presented in Fig. 4, showing results along the centerline for  $y = 0$  mm. Gaseous fuel, whose mass fraction is  $Y_F$ , is injected on the right side of the configuration. It decreases due to diffusion and starts burning close to the stagnation plane in the high temperature region. The flame structure is presented in terms of the gaseous mixture fraction  $Z_g$ , which is here defined with respect to the carbon mass fraction in the gaseous mixture:

$$Z_g = \frac{W_F}{n_{C,F}W_C} \sum_{k=1}^{N_s} n_{C,k} \frac{Y_k W_C}{W_k}, \quad (22)$$

where  $n_{C,k}$  is the number of carbon atoms in species  $k$ . Since for the gaseous flame gaseous fuel is injected with nitrogen at the right side,  $Z_g$  increases monotonically from zero to  $Z_g^F = 0.32$  (Fig. 4(a)). The high temperature region is located around the stagnation plane and the inner reaction zone is identified by the OH mass fraction on the oxidizer side of the configuration, where a stoichiometric mixture is found ( $Z_g^{\text{st}} = 0.063$ ) and the heat is mainly released (not shown).

The structure of the spray flame, presented in Fig. 4(b), is more complex. Due to the selected operating conditions, the droplets that are injected on the right side start evaporating only after they have reached the high temperature region and droplets cannot pass through the stagnation plane since no slip velocity between phases is allowed. The evaporation zone, identified by the mass evaporation source term  $\dot{S}_m$  in Fig. 4(b), is then confined to a small region that overlaps with the mixing layer at the right side of the stagnation plane. The evaporated fuel mass fraction  $Y_F$  then passes through the stagnation plane due to mixing and the reaction zone is identified at the oxidizer side, similarly to the pure gaseous case. The maximum value of the fuel mass fraction is smaller than the maximum value of  $Z_g$ , indicating that  $Y_F$  starts reacting before the end of the evaporation zone. However, the reaction zone where the heat is mainly released is located on the oxidizer side, so that the evaporation layer and the reaction zone do not overlap spatially, confirming Eq. (7). Indeed, the scaling relations (10) are confirmed here: the inner reaction zone (identified by the presence of OH) does not differ between gas and spray flames. The peak of the OH mass fraction is smaller for the spray flame as well as the integral of the fuel consumption rate (not shown), suggesting that a smaller flame speed characterizes the spray flame.

The flame structures for the three values of  $Lf$  considered in this work are compared in the  $Z_g$ -space to the gaseous flame structure in Fig. 5. As seen in Fig. 4(b), for a spray flame the profile of  $Z_g$  is not monotonic in physical space, as a result of the competition between evaporation and mixing. Alternatively, the effective composition space variable proposed in [40] could be used to represent the flame structure along a monotonic direction. Since mixing and evaporation processes overlap spatially, the maximum value of  $Z_g$  is smaller for the spray flames than for the gaseous flame, even if the same amount of fuel has been injected. Its value decreases when  $Lf$  increases, i.e., when the evaporation time increases. The maximum value of the gaseous mixture fraction for the steady solution  $Z_{g,\text{max}}^{\text{steady}}$  is used in the following to normalize the results ( $Z_{g,\text{max}}^{\text{steady}} = 0.319, 0.168, 0.132, 0.096$  for gaseous and spray flames with  $Lf = 0.075, 0.3, 0.675$ , respectively). The effect of the spray on the combustion process is apparent from profiles of temperature and OH mass fraction. By considering the velocity profile, it has been verified that the local strain rate is similar for all flames (not shown). It is noticed that the maximum values of OH and temperature decrease as the Lefebvre number increases and, consequently, is smaller than the corresponding maximum values for the gaseous flames. This is due to the competition of the evaporation time  $\tau_v$  with the characteristic chemical and mixing times, which implies a reduction of the maximum value of  $Z_g$  and a leaner combustion mode, compared to the stoichiometric diffusion-like mode observed for the gaseous flame.

### 4.2. Examples of spray flame-vortex interaction

A pair of symmetric counter-rotating vortices is superimposed to the initial steady-state velocity field. A schematic of the initialization procedure is presented in Fig. 1(b). The ‘‘Hat’’ vortex is used here [28].

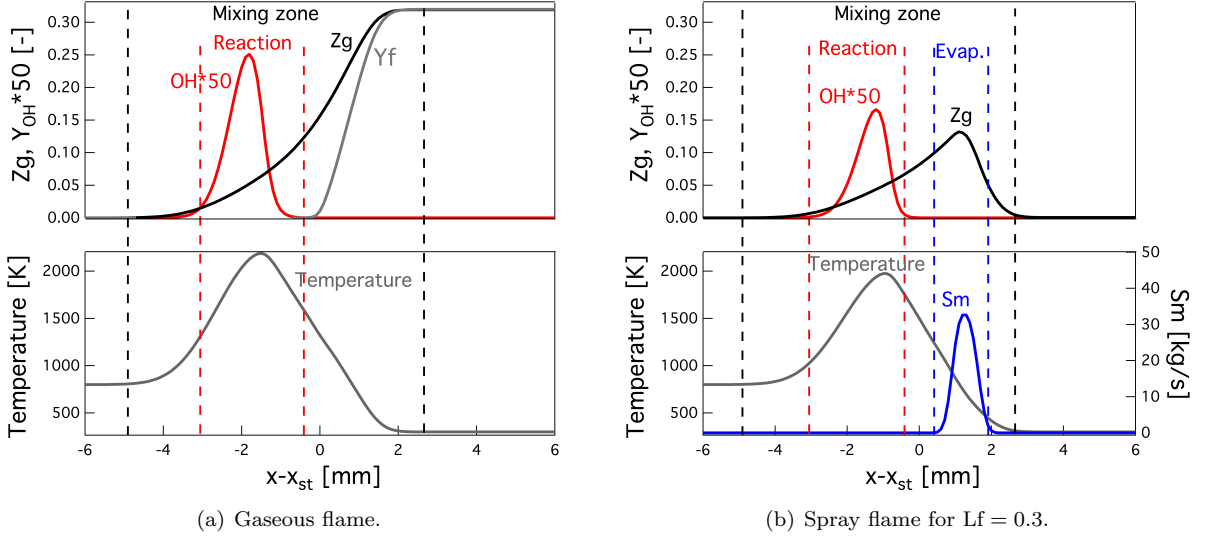


Figure 4: Flame structure at the centerline ( $y = 0$  mm) for (a) gaseous and (b) spray flame. Reaction and mixing zones are identified by the red and black vertical dashed lines, respectively. The evaporation zone is identified by blue vertical dashed lines for the spray flame.  $x_{st}$  is the axial position of the stagnation plane. For clarity, the OH mass fraction is multiplied by a factor 50. (For interpretation of the references to colour in this figure, the reader is referred to the web version of this article.)

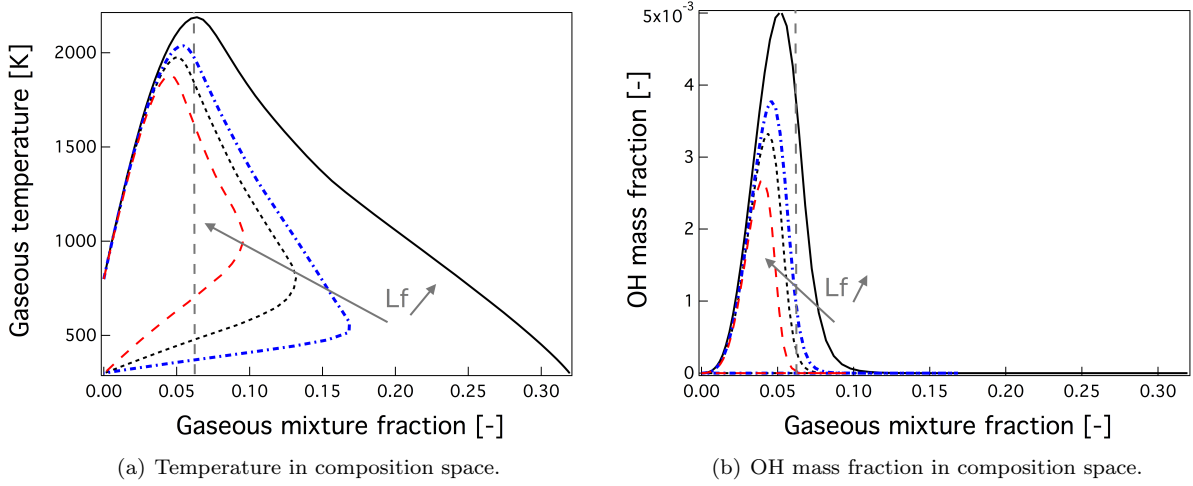


Figure 5: Structure of the steady gaseous (solid line) and spray flames (with increasing Lefebvre number  $Lf = 0.075, 0.3, 0.675$ ) at the centerline ( $y = 0$  mm) in the  $Z_g$ -space. The vertical line indicates the location of stoichiometric mixture fraction. (For interpretation of the references to colour in this figure, the reader is referred to the web version of this article.)

The equation for the velocity field in the vortex reference frame is:

$$u_\theta = \frac{r\Gamma}{r_v^2} \exp\left(-\frac{r^2}{2r_v^2}\right), \quad u_r = 0, \quad (23)$$

where  $r = \tilde{x}/\cos(\theta)$ ,  $\theta = \text{atan}(\tilde{y}/\tilde{x})$ ,  $\tilde{x} = x - x_v$ ,  $\tilde{y} = y - y_v$ , and  $(x_v, y_v)$  is the initial position of the center of the vortex,  $\Gamma$  is the vortex strength and  $r_v$  is the inner vortex radius. The two vortices of equal radii and opposite strengths are initially separated by a distance  $s$  (see Fig. 1), and they are at equal distance

$s/2$  from the symmetry axis  $y = 0$ . As demonstrated in [28], an appreciable tangential velocity  $u_\theta$  induced by the Hat vortex still exists until  $3r_v$  away from the vortex center. Following the recommendations of [28], the separation distance between the two vortices and the flame is set to  $s = l_x = 3r_v$ , to avoid initial interactions between the viscous cores of the vortices and the reaction zone. Using this constraint on the vortex separation distance, the characteristic length scale of the perturbation is therefore  $l_T = 9r_v$ . The vortices that are injected from the left side interact then with the reaction zone before crossing the stagnation plane.

To map the spectral diagram, parametric simulations along isolines of characteristic strain rate  $A_\Gamma$  are performed using the following procedure: first the non-dimensional vortex strength  $\tilde{\Gamma}$  is fixed ( $\tilde{\Gamma} = 1, 2, 4, 6, 10$ ), then the radius of the vortex core is chosen ( $\frac{r_v}{\delta_L} = \frac{1}{18}, \frac{2}{9}, \frac{5}{9}, \frac{10}{9}$ ), determining the value of the characteristic vortex strength from  $\Gamma = A_\Gamma r_v^2$ .

Case	Vortex properties		Flame-vortex interaction			
	$\tilde{\Gamma}$	$r_v/\delta_L$	GAS (Lf=0)	D25 (Lf = 0.075)	D50 (Lf = 0.3)	D75 (Lf = 0.675)
A	1	5/9	no extinction	no extinction	no extinction	no extinction
B	4	5/9	no extinction	flame quenching	flame quenching	flame quenching
C	2	10/9	no extinction	no extinction	fuel depletion	fuel depletion
D	4	3/3	no extinction	no extinction	no extinction	flame quenching
E	2	5/9	no extinction	no extinction	no extinction	fuel depletion

Table 1: Summary of operating conditions and regimes for gaseous and spray flame-vortex interaction configurations.

The presence of the vortex has two effects on a spray flame. First, in analogy to the classical behavior of purely gaseous flames, the vortices wrinkle and strain the flame due to the stretch imposed on the flame front. To illustrate this, we decompose the stretch  $\kappa$  into a local strain rate  $a$  and a curvature contribution:

$$\kappa = \underbrace{(\delta_{ij} - \hat{n}_i \hat{n}_j) \frac{\partial u_i}{\partial x_j}}_{\text{strain}} + \underbrace{S_d \frac{\partial \hat{n}_i}{\partial x_i}}_{\text{curvature}} = a + S_d \nabla \cdot \hat{\mathbf{n}} \quad (24)$$

where  $\hat{\mathbf{n}} = -\nabla Z_g / |\nabla Z_g|$  is the vector normal to the flame surface and  $S_d$  is the displacement speed. Second, the vortices also interact with the droplet dynamics by changing their velocities. The induced droplet preferential concentration due to the centrifugal vortex force may cause a local variation of the gaseous mixture composition. Depending on the strength and dimension of the vortices, the spray flame front may quench by strain rate effects or by the local depletion of fuel. Indeed, for a given Lf number, i.e. initial droplet diameter, the flame-vortex interaction is evaluated for seventeen combinations of  $\tilde{\Gamma} - \text{Pe}_0$ , keeping R constant. The most representative cases for the spray flame-vortex interaction cases are summarized in Table 1.

Results from three different spray-flame-vortex interaction cases for Lf = 0.3 are presented in Figs. 6 (case A), 9 (case B) and 11 (case C). Here, the time is normalized by the time that is required by the vortex core to reach the flame front. The inner reaction zone, identified by the OH isocontours, is colored by the strain rate in the bottom part of the images. The vortex location is represented by vorticity isocontours. The mixture fraction, normalized by its maximum value for the steady case  $Z_g^* = Z_g / (Z_{g,\text{max}}^{\text{steady}})$ , is presented in the bottom part and the spray droplets, shown in the top part, are colored by their axial velocity. The curvature is not shown since its magnitude is smaller than the strain rate and its maximum is generally located at the hat brim of the flame. For conditions at which flame extinction occurs at the symmetry axis<sup>4</sup>, it can be concluded that the contribution of curvature to flame stretch is less relevant compared to the strain rate. The vortex dissipation case is not relevant for the understanding of the spray flame-vortex interaction and is not further discussed.

<sup>4</sup>When differential diffusion effects are accounted for, extinction of gaseous flames is not always located at the hat top [29].

Figure 6 presents the spray-flame-vortex interaction corresponding to  $\tilde{\Gamma} = 1$  and  $r_v/\delta_L = 5/9$  (case A in Table 1). Here, the flame wrinkling is enhanced by the contribution of curvature to the stretch at the hat brim whereas the maximum of the strain rate is detected at the symmetry point of the dome, i.e the hat top. The stretching of the flame due to the vortex interaction is not sufficiently strong to penetrate the flame front. To better visualize the processes, the temporal evolution of the flame and flow quantities at the location corresponding to the hat top are represented in Fig. 7. For comparison, results for the corresponding purely gaseous flames are also shown. The local strain rate on the inner reaction zone of the flame, evaluated at the position of the maximum value of OH, increases with time due to the interaction with the approaching vortices (see Fig. 7(a)).

Considering the local heat release for the reference flame at steady conditions,  $\dot{\omega}_T^{\text{steady}}$ , we introduce the normalized overall heat release at the symmetry axis as:

$$\Omega_T^* = \frac{\int_{-\infty}^{\infty} \dot{\omega}_T dx}{\int_{-\infty}^{\infty} \dot{\omega}_T^{\text{steady}} dx}, \quad (25)$$

which is a global quantity used to analyze the effect of strain on the flame structure. As observed for gaseous flames [30], the mean heat release increases with the vortex strength. However, Fig. 7(a) shows that the vortex strength is not enough in this case to quench the flame. In analogy with gaseous flames, spray flames interacting with a vortex pair sustain higher values of local strain rate compared to the critical strain rate for steady flames due to unsteadiness and curvature effects [4]. The vortices interact also with the spray, by reversing its axial velocity in the evaporation zone near the hat top. Evaporating droplets are pushed away from the flame front, thereby decreasing the maximum value of  $Z_g^*$  available for combustion. For the present case, the contribution from this effect is not significant enough to affect the flame behavior. This process is highlighted in Fig. 7(b), which presents the temporal evolution of the maximum gaseous mixture fraction  $Z_{g,\text{max}}^*$  and of the maximum velocity of the evaporating droplets  $u_{l,\text{max}}$ , located at the centerline  $y = 0$  in the region where  $\dot{S}_m \neq 0$ .

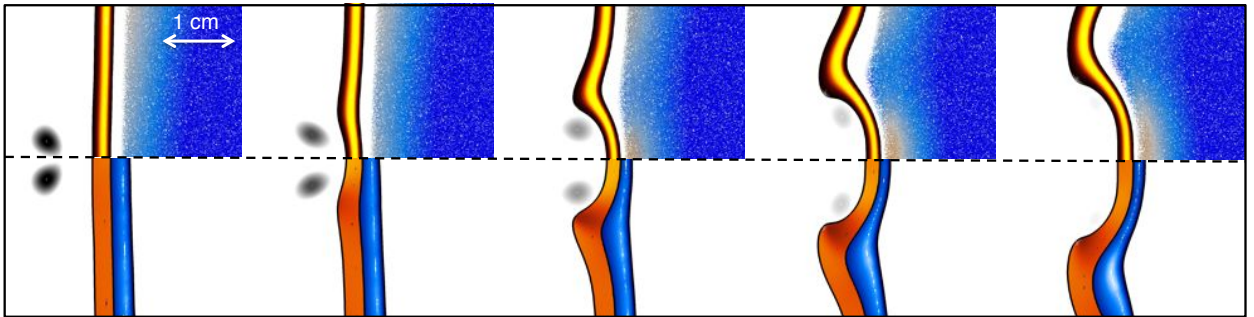
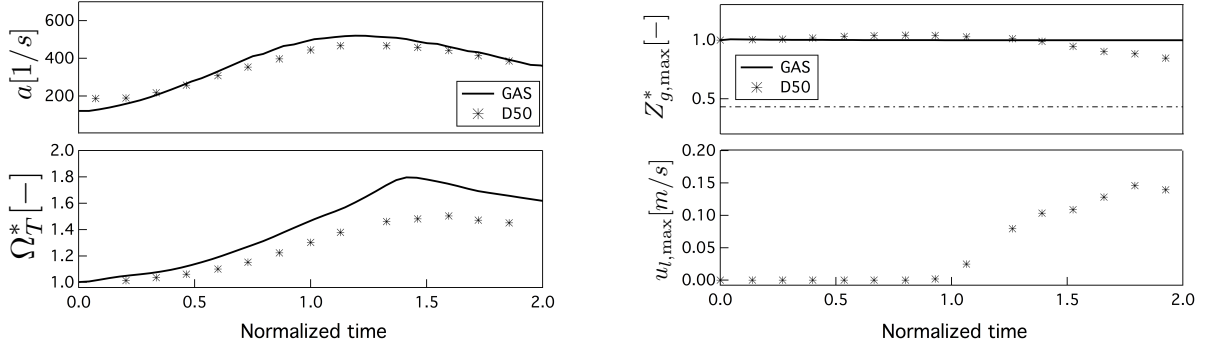


Figure 6: Temporal evolution of the spray-flame-vortex interaction for the case without extinction (case A in Table 1 corresponding to  $r_v/\delta_L = 5/9$ ,  $\tilde{\Gamma} = 1$  and  $Lf = 0.3$ ). Instantaneous fields at normalized time  $\tau = 1.2, 1.4, 1.6, 1.8, 2.0$  (from left to right). Top: isocontours colored by OH mass fraction (black to yellow), vorticity contours (black), droplet positions colored by droplet axial velocity (blue to red dots). Bottom: OH isocontours colored by strain rate (red to yellow), vorticity contours (black) and gaseous mass fraction  $Z_g^*$  (blue). (For interpretation of the references to colour in this figure, the reader is referred to the web version of this article.)

For  $\tilde{\Gamma} = 4$  and  $r_v/\delta_L = 5/9$  (case B in Table 1), presented in Fig. 9, the vortex pair is sufficiently strong to penetrate the flame. The quenching point corresponds to the condition of maximum strain rate, which is located at the symmetry point of the dome. At the moment of quenching, the gaseous mixture fraction distribution is homogeneous. This extinction mode is further analyzed in Fig. 10. The mean heat release increases by a factor of three because of the local strain rate, before the flame quenches at  $a \approx 2800 \text{ s}^{-1}$ . Here, the quenching time is identified by the point at which  $\Omega_T^*$  starts decreasing (represented by the vertical line in Fig. 10). At the same time, the maximum value of  $Z_g^*$  decreases due to the spray flame-vortex interaction.



(a) Strain rate induced on the inner flame zone (top) and normalized mean heat release (bottom) as a function of normalized time.

(b) Maximum value of  $Z_g^*$  (top) and of the evaporating droplets velocity  $u_l$  (bottom) as a function of normalized time.

Figure 7: Temporal evolution for the spray (symbols) and gaseous (lines) flames for the case without extinction at the hat top (case A,  $r_v/\delta_L = 5/9$ ,  $\bar{\Gamma} = 1$  and  $Lf = 0.3$ ). The horizontal dashed line in the upper right panel indicates the stoichiometric condition. (For interpretation of the references to colour in this figure, the reader is referred to the web version of this article.)

However, when the flame extinguishes,  $Z_g^*$  remains higher than the stoichiometric value. Enough gaseous fuel is then available for combustion, confirming the role of the strain rate contribution for this mode of extinction. For the same vortex characteristics, the purely gaseous flame does not quench since the spray flame is more sensitive to strain than the gaseous flame as predicted by the spectral diagram.

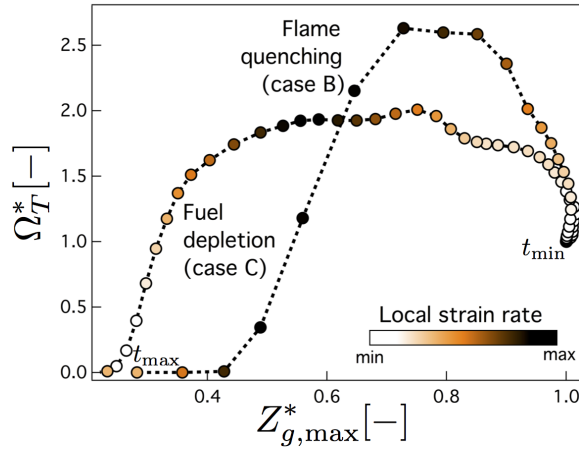


Figure 8: Evolution of  $\Omega_T^*$  as a function of the maximum value of  $Z_g^*$  for case B (flame quenching) and C (fuel depletion). Results are colored by the local strain rate.

For gaseous flames, the response to strain is commonly represented in the  $\Omega_T^*$ - $a$ -space. In order to simultaneously account for the effect on the mixture fraction for spray flames, results are represented in the  $\Omega_T^*$ - $Z_{g,max}^*$ -space, colored by the strain rate. These results are illustrated in Fig. 8. At the initial time, the mixture fraction value coincides with the steady solution. As soon as the strain rate increases, the normalized heat release increase too, and simultaneously, the maximum value of  $Z_g^*$  decreases due to the vortex interaction with the spray. For higher values of the strain rate, the total heat release drastically decreases since the flame quenches. The local value of  $Z_{g,max}^*$  is still higher than the stoichiometric value  $Z_{g,max}^{*,stoch} = 0.478$ , indicating that in this case the quenching is due to strain rate since enough fuel is available to sustain the diffusion flame.

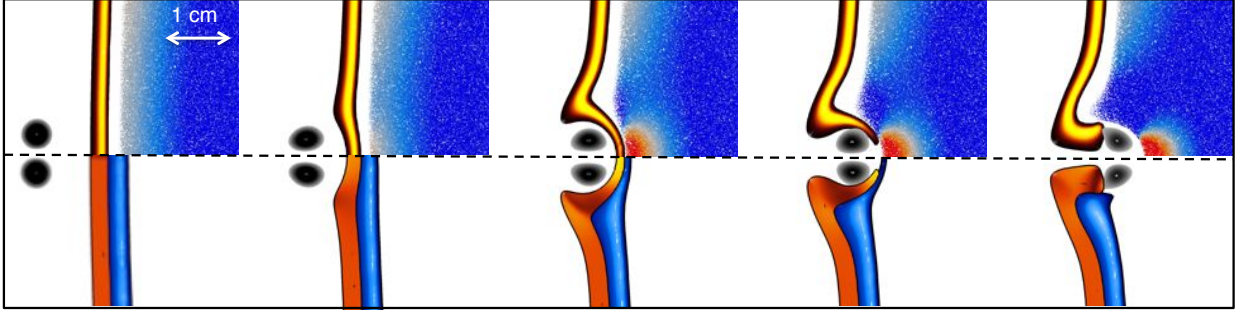
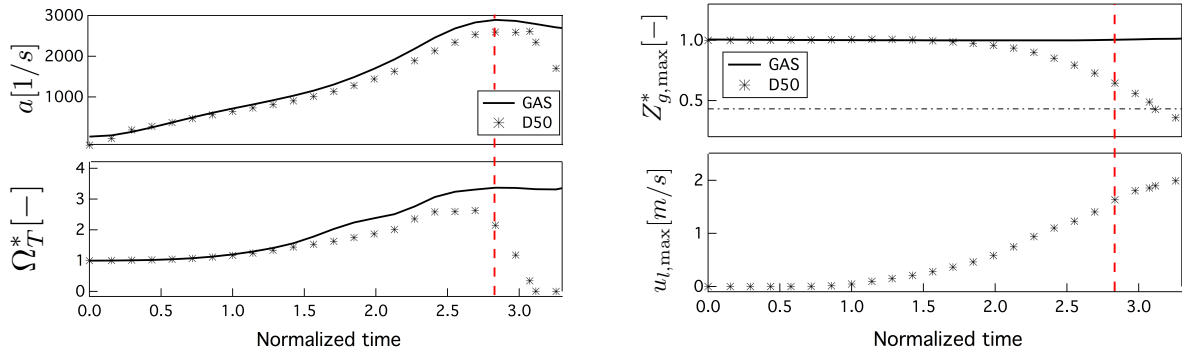


Figure 9: Temporal evolution of the spray flame-vortex interaction for the case with extinction due to strain rate (case B in Table 1 corresponding to  $r_v/\delta_L = 5/9$ ,  $\tilde{\Gamma} = 4$  and  $Lf = 0.3$ ). Instantaneous fields at normalized time  $\tau = 0.0, 2.4, 2.8, 3.25, 3.5$  (from left to right). Legend is the same as in Fig. 6.



(a) Strain rate induced on the inner flame zone (top) and normalized mean heat release (bottom) as a function of normalized time. (b) Maximum value of  $Z_g^*$  (top) and of the evaporating droplets velocity (bottom) as a function of normalized time.

Figure 10: Temporal evolution for the spray (symbol) and gaseous (line) flames for  $r_v/\delta_L = 5/9$ ,  $\tilde{\Gamma} = 4$  and  $Lf = 0.3$  (case B) at the hat top. The horizontal line in the upper right panel indicates the stoichiometric mixture fraction, the vertical line denotes the time at flame quenching.

Figure 11 corresponds to case C in Table 1 ( $\tilde{\Gamma} = 2$  and  $r_v/\delta_L = 10/9$ ). For this case, the strain rate at the hat top is not strong enough to quench the flame and the depletion of gaseous fuel is the primary reason for extinction. This extinction mechanism is not present in the classical gaseous flame-vortex configuration. Looking at the axial velocity of the droplets, it can be seen that the vortices induce a strong positive velocity to the droplets located close to the hat top and a strong negative velocity to the droplets near the hat brim. Indeed, the droplets are forced to leave the hat top region to reach the hat brim of the flame, leading to a strong preferential droplet concentration along the flame. This translates into local inhomogeneities of the gaseous mixture composition, which is apparent when looking at the gaseous mixture fraction  $Z_g^*$  in Fig. 11. The mixture fraction accumulates at the hat brim, exceeding the maximum value of  $Z_g^*$  observed for the steady case, whereas its concentration decreases at the hat top with time. As such, the flame is not sustained anymore by fuel supply and, consequently, extinguishes.

The same conclusions can be drawn by considering the temporal evolution of strain rate and heat release in Fig. 12. After an increase in  $\Omega_T^*$  due to the strain rate, a plateau is reached for both strain rate and  $\Omega_T^*$ . At this time, the maximum value of  $Z_g^*$  decreases due to the spray-vortex interaction. For  $Z_g^*$  smaller than the stoichiometric value,  $\Omega_T^*$  starts to decrease due to fuel depletion (identified by the vertical line). Fuel depletion is then observed in a region where the strain rate decreases, confirming that the extinction is not

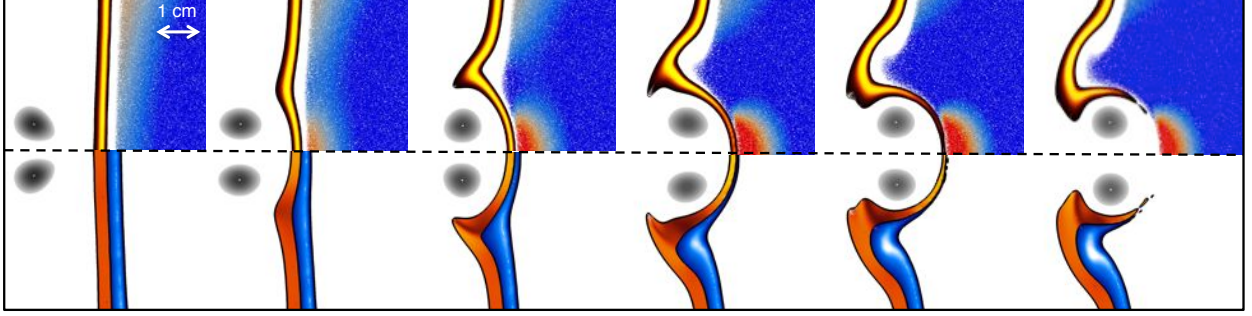
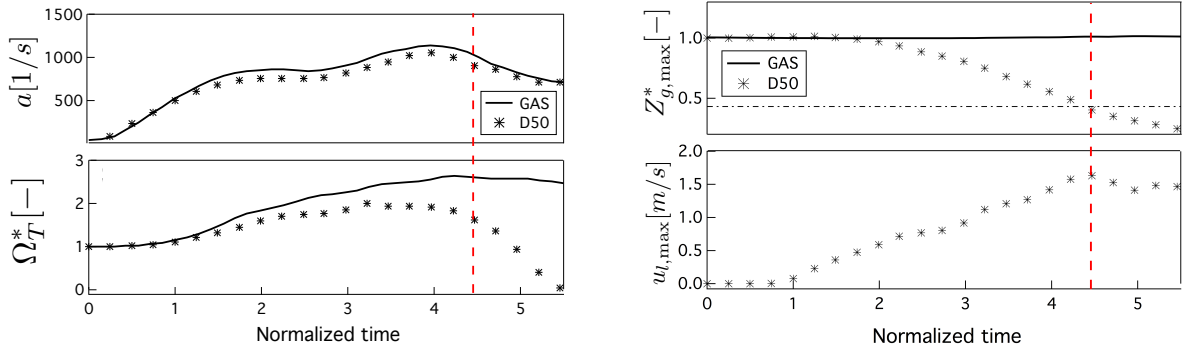


Figure 11: Temporal evolution of the spray-flame-vortex interaction for the case of extinction due to fuel depletion (case C in Table 1 corresponding to  $r_v/\delta_L = 10/9$ ,  $\tilde{\Gamma} = 2$  and  $Lf = 0.3$ ). Instantaneous fields at normalized time  $\tau = 1.0, 2.25, 3.5, 4.75, 5.25, 5.35$  (from left to right). Legend is the same as in Fig. 6.



(a) Strain rate induced on the inner flame zone (top) and normalized mean heat release (bottom) as a function of normalized time. (b) Maximum value of  $Z_g^*$  (top) and the evaporating droplets velocity (bottom) as a function of normalized time.

Figure 12: Temporal evolution for the spray (symbol) and gaseous (line) flames for the case of extinction due to fuel depletion at the hat top (case C,  $r_v/\delta_L = 10/9$ ,  $\tilde{\Gamma} = 2$  and  $Lf = 0.3$ ). The horizontal line in the upper right panel indicates the stoichiometry, the vertical line denotes the time of fuel depletion.

due to strain rate but due to a decrease of  $Z_g^*$ . This behavior is clearly identified by looking at the solution in the  $\Omega_T^*-Z_{g,\max}^*$  space which has been added to Fig. 8. Increasing the strain rate and decreasing  $Z_g^*$  has an opposite effect on the flame. Starting at the right side (at  $Z_g^* = 1$ ),  $\Omega_T^*$  initially increases since the positive contribution of the strain rate on  $\Omega_T^*$  dominates over the adverse effect due to the decrease of  $Z_g^*$ . For the fuel depletion case, a plateau is reached when the spray-vortex interaction compensates the flame-vortex interaction. After this, the flame extinguishes when  $Z_{g,\max}^*$  becomes smaller than the stoichiometric value and is not enough to sustain combustion after the maximum of the local strain rate has passed.

This extinction mode due to fuel depletion is not observed for purely gaseous flames since it is due to the interaction of the vortices with the spray, causing an inhomogeneous distribution of evaporated gaseous fuel.

By looking at the solutions in the  $\Omega_T^*-Z_{g,\max}^*$  space, it is then possible to distinguish flame quenching from the fuel depletion case. The composition trajectory for the flame quenching case by strain rate exhibits a rapid increase followed by a sudden drop in  $\Omega_T^*$  due to strain rate and quenching, respectively. On the contrary, the fuel depletion case C shows the existence of an extended plateau and  $\Omega_T^*$  drops with decreasing strain rate. The evolution of  $\Omega_T^*$  in composition space is used in the following to distinguish between the two extinction modes. However, it is noted that since the vortex passage enhances both fuel depletion and flame quenching, the two extinction modes may not always be easily discriminated.

Simulation results for the 17 operating conditions considered are summarized in the spectral diagram in Fig. 13. Good agreement between the numerical results and the spectral diagram, derived from the time scale analysis, is observed for both flame configurations. The injection of fuel as spray reduces the flame robustness, since its quenching time is larger compared to that of the purely gaseous phase due to the evaporation time. Such behavior is taken into account by the spectral diagram and was confirmed from the numerical results. Furthermore, a new extinction mode is identified for spray flames. Due to the underlying physical processes that are responsible for this extinction process, this mode is restricted to spray flames and not observed in gaseous flames. The competition between processes associated with the evaporation leads to a local depletion of fuel, which is illustrated in the spectral diagram (Fig. 13(b)).

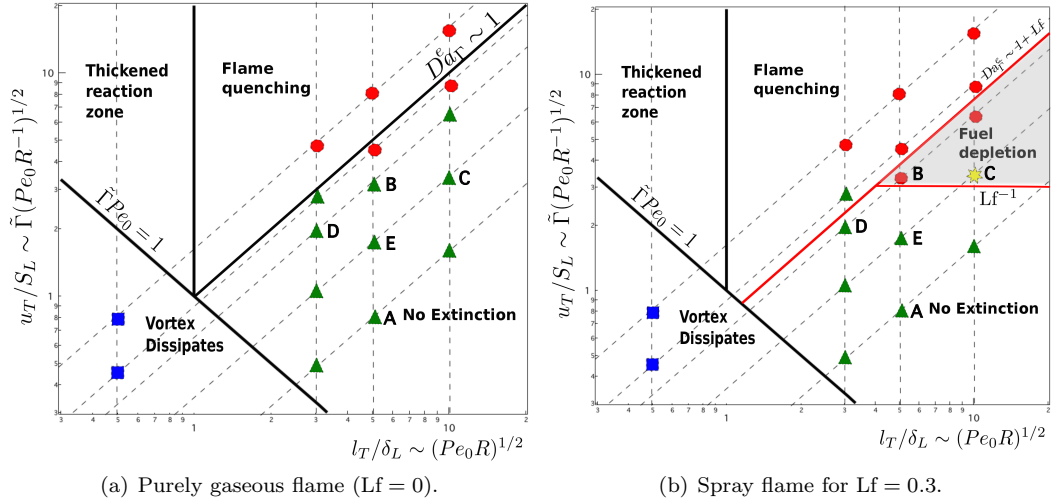


Figure 13: Spectral diagram for flame-vortex interaction: the symbols represent numerical simulations. Squares represent the vortex dissipation regime, triangles the “no extinction” condition, circles the extinction due to strain rate, stars are for extinction due to fuel depletion. The new fuel depletion zone is highlighted in gray.

### 4.3. Effect of Lefebvre number

In the previous section, the role of the evaporation process has been discussed by comparing the response of the flame to the vortex passage for a purely gaseous flame and a spray flame. To fully quantify the effect of the evaporation process, the cases of three  $Lf$  numbers are compared in this section, for constant values of  $Pe_0$  and  $\tilde{\Gamma}$  couple, i.e. only the initial droplet diameter is modified (once again,  $R$  is kept constant in all calculations).

In Figs. 14 and 15, the evolution of  $\Omega_T^*$  is presented as a function of  $Z_{g,max}^*$  for the cases summarized in Table 1. In Fig. 14(a) (case B), the vortex strength is high enough to quench the flame, characterized by a strong increase in  $\Omega_T^*$  followed by a rapid drop, irrespectively of the  $Lf$  number. As discussed in Section 2, the robustness of a spray flame depends on the competition between time scales associated with the chemistry and the evaporation. Indeed, a vortex may quench a spray flame that is characterized by a slow evaporation process and does not extinguish a flame with smaller droplets. This is clearly observed for case D (Fig. 14(b)), for which only the spray flame with the largest  $Lf$  number extinguishes. The spectral diagram suggests that the flame robustness reduces accordingly with  $1 + Lf$ .

On the contrary, the extinction by fuel depletion depends on the competition between advection, mixing and evaporation processes. For larger droplets, the evaporation process is slow and not enough fuel is supplied by the evaporation before the droplets are pushed away from the flame front due to the vortex passage. This is verified in Fig. 15. Depending on the vortex characteristics, fuel depletion is observed for large droplets but not for the smallest (cases C and E). The strong effect of the vortices on the spray distribution is enhanced by the zero slip assumption used in the numerical simulation. For small droplets,

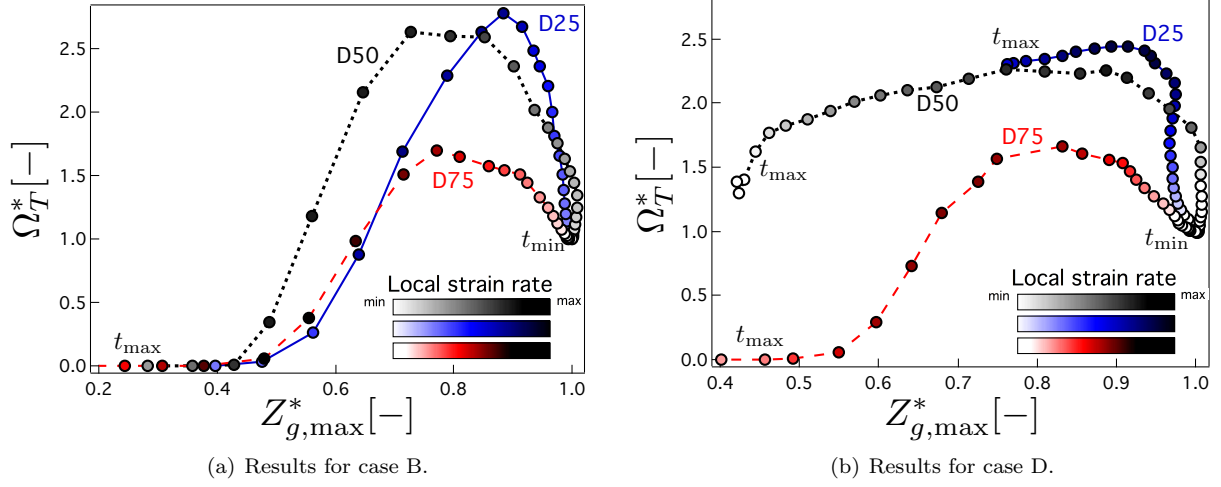


Figure 14: Flame quenching: Evolution of  $\Omega_T^*$  as a function of the maximum value of  $Z_g^*$  for  $Lf = 0.075$  (blue),  $Lf = 0.3$  (black),  $Lf = 0.675$  (red), colored by the local strain rate. (For interpretation of the references to colour in this figure, the reader is referred to the web version of this article.)

this assumption is expected to be verified and, in general, the velocity induced by the vortex on the gaseous phase is an order of magnitude larger than the droplet velocity, rapidly forcing the droplets to move with the gaseous field.

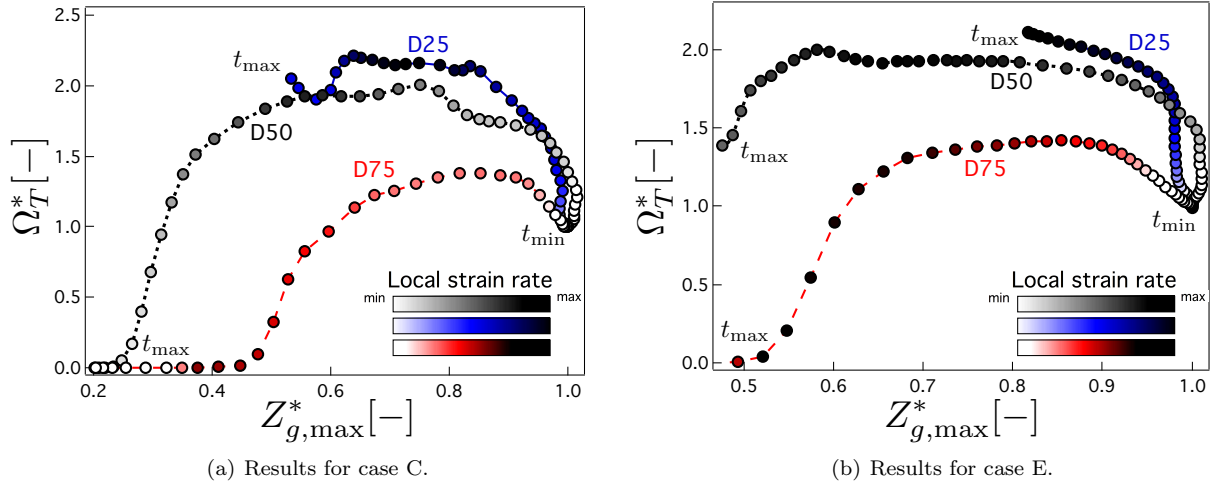


Figure 15: Fuel depletion: evolution of  $\Omega_T^*$  as a function of  $Z_{g,max}^*$   $Lf = 0.075$  (blue),  $Lf = 0.3$  (black),  $Lf = 0.675$  (red), colored by the local strain rate. (For interpretation of the references to colour in this figure, the reader is referred to the web version of this article.)

Results for  $Lf = 0.075$  and  $Lf = 0.675$  are compared to the spectral diagram prediction in Fig. 16. By comparing the results to the one obtained for  $Lf = 0.3$  in Fig. 13(b), the dependence of the extinction limit to the  $Lf$  number is verified, the extinction region being extended as the droplet diameter at injection increases. Moreover, concerning the fuel depletion region, the same trend is found: increasing the  $Lf$  number at injection enlarges this region, which is confirmed by our theoretical analysis. By extrapolating the results

to larger  $L_f$  numbers, it is expected that the spray flame with large droplet diameter at injection will be extinguished by any vortex that reaches the reaction zone, since the flame will be too close to extinction.

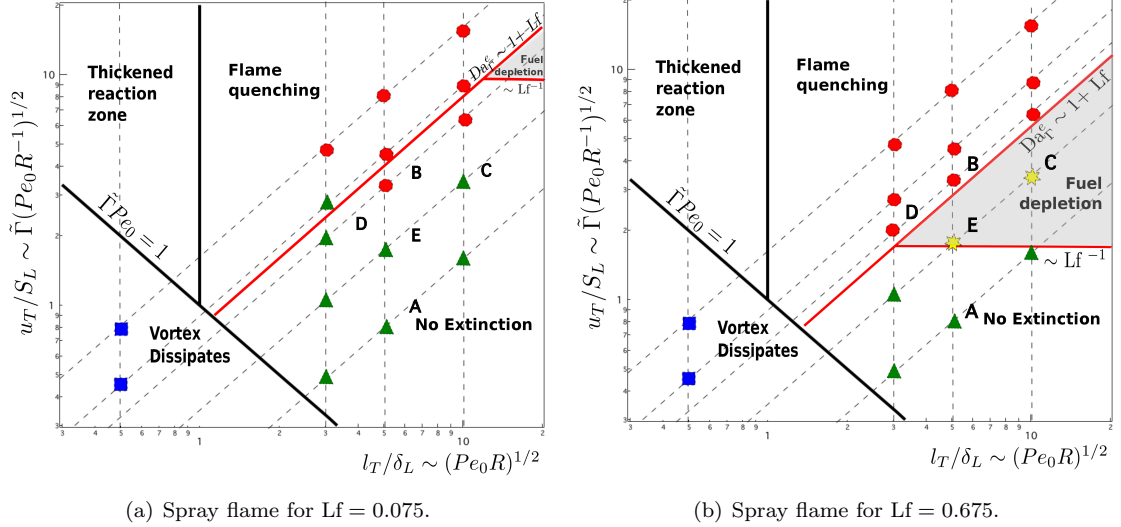


Figure 16: Spectral diagram for spray-flame-vortex interaction: the symbols represent numerical simulations. Squares represent the vortex dissipation regime, triangles the “no extinction” mode, circles the extinction due to strain rate, stars are for extinction due to fuel depletion. The new extinction regime due to fuel depletion is shown in gray. (For interpretation of the references to colour in this figure, the reader is referred to the web version of this article.)

## 5. Conclusions

The spectral diagram for gaseous flame-vortex interaction was extended to spray flames. An analytic derivation was presented in the limit of momentum equilibrium, considering the influence of the evaporation time on the flame quenching time. A third dimension has been added to the spectral diagram, identified by the ratio between evaporation and chemical times, which is represented by the Lefebvre number,  $L_f$ . To confirm the spectral diagram, numerical simulations were performed by considering a planar counterflow configuration using a detailed chemistry description, and a Lagrangian method to describe the droplet evolution.

Two different extinction modes were identified. The flame quenching, caused by an induced high strain rate at the flame front, is commonly observed for purely gaseous flames. The fuel depletion, a new extinction mode that is particular to spray flames, was caused by a local lack of gaseous fuel due to the preferential droplet concentration induced by the vortex interaction with the spray. The newly developed spectral diagram for spray flames accounts for both effects and correctly describes the numerical results. The effect of the evaporation time on the flame-vortex interaction and, specifically, on these two extinction modes was quantified by examining spray flames with different values of the  $L_f$  number. The proposed spectral diagram establishes the framework for the analysis of spray flame-vortex interaction to obtain a fundamental understanding of spray turbulent combustion and to develop turbulent spray combustion models, which require the correct representation of both extinction modes. To account for slip velocity effects on spray-flame-vortex interactions, the spectral diagram should be generalized to large drag Stokes numbers. Also, further extensions are required to consider vortex injection at the fuel side.

## Acknowledgments

The authors gratefully acknowledge financial support through NASA with Award Nos. NNX14CM43P and NNM13AA11G and Prof. Heinz Pitsch for permission to use his code for this analysis. The resources

of the National Energy Research Scientific Computing Center, which is supported by the Office of Science of the U.S. Department of Energy under Contract No. DE-AC02-05CH11231, are also acknowledged.

## References

- [1] P. H. Renard, D. Thévenin, J. C. Rolon, and S. Candel. Dynamics of flame/vortex interactions. *Prog. Energy Combust. Sci.*, 26:225–282, 2000.
- [2] F. A. Williams. *Combustion Theory*. Benjamin Cummings, Menlo Park, CA, 1985.
- [3] R. Borghi. Turbulent combustion modelling. *Prog. Energy Combust. Sci.*, 14:245–292, 1988.
- [4] T. Poinsoot and D. Veynante, and S. Candel. Quenching processes and premixed turbulent combustion diagrams. *J. Fluid Mech.*, 228:561–605, 1991.
- [5] N. Peters. Laminar diffusion flamelet models in non-premixed turbulent combustion. *Prog. Energy Combust. Sci.*, 10:319–339, 1984.
- [6] N. Peters. Laminar flamelet concepts in turbulent combustion. *Proc. Combust. Inst.*, 21:1231–1250, 1988.
- [7] R. W. Bilger. The structure of turbulent non-premixed flames. *Proc. Combust. Inst.*, 22:475–488, 1989.
- [8] T. Poinsoot and D. Veynante. *Theoretical and Numerical Combustion, Third Edition*. 2012.
- [9] O. Colin, F. Ducros, D. Veynante, and T. Poinsoot. A thickened flame model for large eddy simulations of turbulent premixed combustion. *Phys. Fluids*, 12(7):1843–1863, 2000.
- [10] B. Cuenot and T. Poinsoot. Effect of curvature and unsteadiness in diffusion flames. Implications for turbulent diffusion flames. *Proc. Combust. Inst.*, 25:1383–1390, 1994.
- [11] M. Vera, M. Hermanns, and A. Liñán. A combustion diagram to characterize the regimes of interaction of non-premixed flames and strong vortices. *3<sup>rd</sup> European Combustion Meeting*, 2007.
- [12] A. Liñán, M. Vera, and A. L. Sanchez. Ignition, liftoff, and extinction of gaseous diffusion flames. *Annu. Rev. Fluid Mech.*, 47:293–314, 2015.
- [13] K. Luo, H. Pitsch, M. G. Pai, and O. Desjardins. Direct numerical simulations and analysis of three-dimensional n-heptane spray flames in a model swirl combustor. *Proc. Combust. Inst.*, 33:667–674, 2011.
- [14] A. Vie, B. Franzelli, Y. Gao, T. Lu, H. Wang, and M. Ihme. Analysis of segregation and bifurcation in turbulent spray flames: A 3d counterflow configuration. *Proc. Combust. Inst.*, 35:1675–1683, 2014.
- [15] V.S. Santoro, D.C. Kyritsis, and A. Gomez. An experimental study of vortex-flame interaction in counterflow spray diffusion flames. *Proc. Combust. Inst.*, 28:1023–1030, 2000.
- [16] V.S. Santoro and A. Gomez. Extinction and reignition in counterflow spray diffusion flames interacting with laminar vortices. *Proc. Combust. Inst.*, 29:585–592, 2002.
- [17] A. Lemaire, T. R. Meyer, K. Zähringer, J. R. Gord, and J. C. Rolon. PIV/PLIF investigation of two-phase vortex-flame interactions. *11th Int. Symp. on Applications of Laser Techniques to Fluid Mechanics*, July 8-11 2002.
- [18] A. Lemaire, K. Zähringer, T. R. Meyer, and J. C. Rolon. Unsteady effects on flame extinction limits during gaseous and two-phase flame/vortex interactions. *Proc. Combust. Inst.*, 30:475–483, 2005.
- [19] S.-M. Shiah and M. Sichel. On the interaction of a dense spray diffusion flame and a potential vortex. *AIAA Paper 93-0901*, 1993.
- [20] E. Fernández-Tarrazo, M. Vera, and A. Liñán. Liftoff and blowoff of a diffusion flame between parallel streams of fuel and air. *Combust. Flame*, 144:261–276, 2008.
- [21] B. Michaelis and B. Rogg. Fem-simulation of laminar flame propagation II: twin and triple flames in counterflow. *Combust. Sci. Tech.*, 177:955–78, 2005.
- [22] J. Réveillon and L. Vervisch. Analysis of weakly turbulent diluted-spray flames and spray combustion regimes. *J. Fluid Mech.*, 537:317–347, 2005.
- [23] F.E. Marble. Dynamics of dusty gases. *Annu. Rev. Fluid Mech.*, 2:397–446, 1970.
- [24] D. R. Ballal and A. H. Lefebvre. Flame propagation in heterogeneous mixtures of fuel droplets, fuel vapor and air. *Proc. Combust. Inst.*, 18:321–327, 1981.
- [25] J. M. Senoner. *Large Eddy Simulation of the Two Phase Flow in an Aeronautical Burner using the Euler-Lagrange Approach*. PhD thesis, INP Toulouse, 2010.
- [26] A. Dvorjetski and J. B. Greenberg. Steady-state and extinction analyses of counterflow spray diffusion flames with arbitrary finite evaporation rate. *Combust. Sci. Tech.*, 174(8):187–208, 2002.
- [27] M. Hermanns, M. Vera, and A. Liñán. On the dynamics of flame edges in diffusion-flame/vortex interactions. *Combust. Flame*, 149:32–48, 2007.
- [28] T. Mantel, J. M. Samaniego, and C. T. Bowman. Fundamental mechanisms in premixed turbulent flame propagation via vortex-flame interactions - part II: numerical simulation. *Combust. Flame*, 118(4):557–582, 1999.
- [29] V. R. Katta, C. D. Carter, G. J. Fiechtner, W. M. Roquemore, J. R. Gord, and J. C. Rolon. Interaction of a vortex with a flat flame formed between opposing jets of hydrogen and air. *Proc. Combust. Inst.*, 27:587–594, 1998.
- [30] P. H. Renard, J. C. Rolon, D. Thévenin, and S. Candel. Investigations of heat release, extinction and time evolution of the flame surface, for a nonpremixed flame interacting with a vortex. *Combust. Flame*, 117(3):189–205, 1999.
- [31] D. Thévenin, P. H. Renard, J. C. Rolon, and S. Candel. Extinction processes during a non-premixed flame vortex interaction. *Proc. Combust. Inst.*, 27:719–726, 1998.
- [32] A. L. Sanchez, J. Urzay, and A. Liñán. The role of separation of scales in the description of spray combustion. *Proc. Combust. Inst.*, 35:1549–1577, 2014.

- [33] R. Miller and J. Bellan. Direct numerical simulation of a confined three-dimensional gas mixing layer with one evaporating hydrocarbon-droplet-laden stream. *J. Fluid Mech.*, 384:293–338, 1999.
- [34] C. Crowe, M. Sharma, and D. Stock. The particle-source-in cell (PSI-CELL) model for gas-droplet flows. *J. Fluids Eng.*, 99(2):325–332, 1977.
- [35] B. Sirjean, E. Dames, D. A. Sheen, and H. Wang. Simplified chemical kinetic models for high-temperature oxidation of C1 to C12 n-alkanes. 6th US National Combustion Meeting, 2009. Paper 23F1.
- [36] O. Desjardins, G. Blanquart, G. Balarac, and H. Pitsch. High order conservative finite difference scheme for variable density low Mach number turbulent flows. *J. Comput. Phys.*, 227(15):7125–7159, 2008.
- [37] Shashank. *High Fidelity Simulation of Reactive Liquid Fuel Jets*. PhD thesis, Stanford University, 2012.
- [38] A. H. Baker, R. D. Falgout, T. V. Kolev, and Yang U. M. Scaling hypre’s Multigrid Solvers to 100,000 Cores. In *High Performance Scientific Computing: Algorithms and Applications*. Springer, 2012.
- [39] P. N. Brown, G. D. Byrne, and A. C. Hindmarsh. VODE, A Variable-Coefficient ODE Solver. *SIAM J. Sci. Stat. Comput.*, 10:1038–1051, 1989.
- [40] B. Franzelli, A. Vié, and M. Ihme. Generalized composition space formulation for spray flames: monotonic mixing describing variable and associated flamelet model. *Combust. Theory Model.*(in review), 2016.

## Nomenclature

### Dimensionless Numbers

<i>Symbol</i>	<i>Description</i>	<i>Definition/Units</i>
Da	Damköhler number	$\tau_c A_0$
Da <sup>e</sup>	Damköhler number at extinction	$\frac{A_e}{A_\Gamma}$
Lf	Lefebvre number	$\frac{\tau_v}{\tau_c}$
Nu	Nusselt number	$\frac{hd_0}{\lambda}$
Pe <sub>0</sub>	Peclet number of the unperturbed flow	$\frac{A_0 r_0^2}{D_{th}}$
Pr	Prandtl number	$\frac{\nu}{D_T}$
Re <sub>Γ</sub>	Reynolds number based on the vortex strength	
R	Robustness of the flame	$\frac{A_e}{A_0}$
Sc	Schmidt number	$\frac{\nu}{D}$
Sh	Sherwood number	$\frac{kd_0}{D}$
St <sub>p</sub>	Stokes number based on droplet drag time and characteristic flow time	$a\tau_p$
St <sub>v</sub>	Stokes number based on droplet evaporation time and characteristic flow time	$a\tau_v$
St <sub>v,Γ</sub>	Stokes number based on the droplet evaporation time and characteristic vortex time	$A_\Gamma \tau_v$

### Greek Symbols

$\delta_L$	Flame thickness	m
$\delta_{ij}$	Kronecker delta function	–

$\Delta V$	Control volume	$\text{m}^3$
$\Gamma$	Vortex strength	$\text{m}^2 \text{s}^{-1}$
$\tilde{\Gamma}$	Non-dimensional vortex strength	—
$\kappa$	Stretch rate	$\text{s}^{-1}$
$\lambda$	Thermal conductivity of the gas phase	$\text{W m}^{-1} \text{K}^{-1}$
$\mu$	Dynamic viscosity of the gaseous mixture	$\text{kg m}^{-1} \text{s}^{-1}$
$\mathbf{n}$	Unit vector normal to the flame	—
$\nu$	Kinematic viscosity of the gaseous mixture	$\text{m}^2 \text{s}^{-1}$
$\dot{\omega}_k$	Net production rate of species $k$	$\text{kg m}^{-3} \text{s}^{-1}$
$\dot{\omega}_T$	Heat release	$\text{kg K m}^{-3} \text{s}^{-1}$
$\dot{\Omega}_T^*$	Overall heat release at symmetry axis normalized by the steady reference value	—
$\rho$	Gas density	$\text{kg m}^{-3}$
$\rho_l$	Liquid density	$\text{kg m}^{-3}$
$\sigma$	Viscous stress tensor of the gas phase	$\text{s}^{-1}$
$\tau_c$	Chemical time scale	$\text{s}$
$\tau_p$	Droplet relaxation time	$\text{s}$
$\tau_q$	Quenching time scale	$\text{s}$
$\tau_v$	Droplet evaporation time	$\text{s}$
$\theta$	Angular coordinate in the vortex reference frame	$\text{rad}$

**Roman Symbols (Lower case)**

$a$	Local strain rate	$\text{s}^{-1}$
$c_l$	Heat capacity of the liquid phase	$\text{J kg}^{-1} \text{K}$
$c_p$	Heat capacity of the gas phase	$\text{J kg}^{-1} \text{K}$
$d_0$	Droplet diameter at injection	$\text{m}$
$\mathbf{f}_d$	Drag force acting on droplets	$\text{N}$
$f_1$	Drag coefficient	—
$f_2$	Correction factor for heat exchange	—
$f_\infty$	Ratio between laminar flame speed and propagation speed of triple flame	—
$h_k$	Enthalpy of species $k$	$\text{J m}^{-3}$
$l_T$	Characteristic vortex length	$\text{m}$
$l_v$	Latent heat of vaporization	$\text{J kg}^{-1}$

$m_d$	Droplet mass	kg
$n_{C,k}$	Number of carbon atoms of species $k$	—
$p$	Pressure	Pa
$p_s$	Saturated pressure	Pa
$r$	Radial coordinate in vortex reference frame	m
$r_0$	Radius of the vortex ring	m
$r_v$	Inner radius of a vortex	m
$\dot{S}$	Source term induced by the spray	$\text{kg m}^{-3} \text{s}^{-1}$
$s$	Separation distance between counter-rotating vortices	m
$\mathbf{u}_d$	Droplet velocity	$\text{m s}^{-1}$
$u_i$	$i^{\text{th}}$ component of the gas velocity	$\text{m s}^{-1}$
$u_T$	Characteristic speed of the vortex	$\text{m s}^{-1}$
$\mathbf{x}_d$	Droplet position	m
$\tilde{x}$	Physical coordinate in the injection direction in the vortex reference frame	m
$x$	Physical coordinate in the injection direction	m
$x_i$	Physical coordinate in the $i^{\text{th}}$ direction	m
$x_v$	Initial position of the vortex in the injection direction	m
$x_{st}$	Axial position of the stagnation plane	m
$\tilde{y}$	Physical coordinate normal to the injection direction in the vortex reference frame	m
$y$	Physical coordinate normal to the injection direction	m
$y_v$	Initial position of the vortex normal to the injection direction	m
<b>Roman Symbols (Upper case)</b>		
$A_0$	Unperturbed flow strain rate	$\text{s}^{-1}$
$A_e$	Critical extinction strain rate	$\text{s}^{-1}$
$A_\Gamma$	Strain rate induced by the vortex	$\text{s}^{-1}$
$B_M$	Spalding number	-
$D_k$	Molecular diffusivity of species $k$	$\text{m}^2 \text{s}^{-1}$
$D_{th}$	Thermal diffusivity	$\text{m}^2 \text{s}^{-1}$
$L_x$	Separation distance between injectors	m
$L_y$	Vertical domain length	m
$N_s$	Total number of species	—

$S_d$	Displacement speed	$\text{m s}^{-1}$
$S_L$	Laminar flame speed	$\text{m s}^{-1}$
$T$	Temperature of the gas phase	K
$T_d$	Droplet temperature	K
$U_F$	Flame-front velocity	$\text{m s}^{-1}$
$W$	Molecular weight of the mixture	$\text{kg mol}^{-1}$
$W_k$	Molecular weight of species $k$	$\text{kg mol}^{-1}$
$Y_k$	Mass fraction of species $k$	
$Z_g$	Gaseous mixture fraction	—

### A. Effect of the vortex injection side on flame-vortex interaction

In analogy to the theory for gaseous flames, the spectral diagram was developed and numerically verified by considering the vortex injection at the oxidizer side of the configuration. To examine the effect of injecting the vortex pair at the fuel side we performed additional calculations. Typical results for the spray flames when vortices are injected on the fuel side are represented in Fig. 17. The flame is more likely to conform with the fuel depletion extinction since the vortices interact with the spray distribution from the beginning. Due to the presence of the vortices, a strong inverse droplet velocity is observed at the symmetry axis (cfr. Fig. 17(b)), leading to strong inhomogeneities in the  $Z_g^*$ -field. Indeed, for case E fuel depletion is observed when injecting the vortices at the fuel side whereas the flame does not extinguish for an oxidizer side injection of the vortices. Moreover, the spray flame is found to be more sensitive to the strain rate when vortices are injected on the fuel side. This was also observed for gaseous flames (not shown). The spectral diagram does not account for the effect of injection side neither for gaseous nor for spray flames but it still provides a reasonable estimation of the flame behavior based on the order of magnitude of the competing processes in a flame-vortex interaction.

### B. A-priori evaluation of the reference evaporation time scale

The reference evaporation time scale is evaluated following the work of [22], in which the authors suggested the following definition:

$$\tau_v = \frac{\text{Sc} \rho_l d_0^2}{4 \text{Sh} \mu \ln(\text{B}_M^0 + 1)} \quad (26)$$

where Sc is the Schmidt number, Sh is the Sherwood number, and  $\text{B}_M^0 = \text{B}_M(T = T_{burnt}, Y_F = 0, p = 1 \text{ bar})$  is the Spalding number:

$$\text{B}_M^0 = \frac{Y_{F,vs} - Y_F}{1 - Y_{vs}}. \quad (27)$$

The burnt gas temperature is denoted by  $T_{burnt}$  and  $Y_{vs}$  is the mass fraction of gaseous fuel at the droplet surface:

$$Y_{F,vs} = \frac{p_s}{p_s + (1 + p_s) \frac{W_F}{W}}, \quad (28)$$

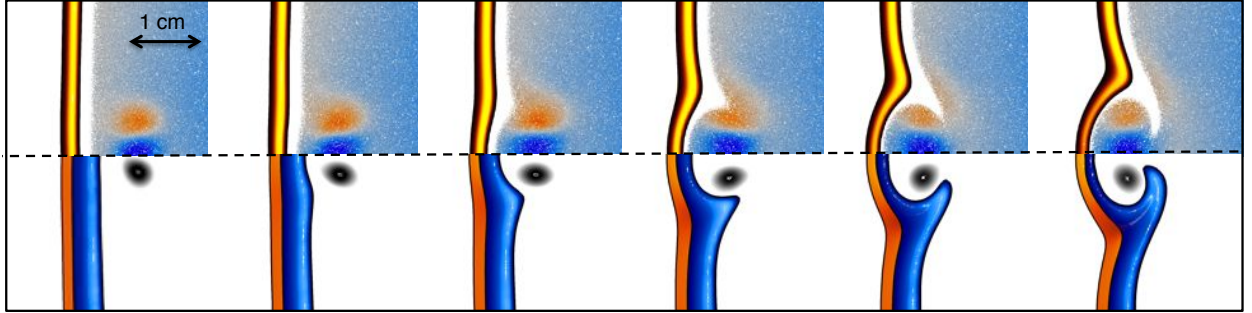
and  $p_s$  is the saturated pressure:

$$p_s = \exp \left\{ \frac{l_v W_F}{R} \left( \frac{1}{T_b} - \frac{1}{T_d} \right) \right\}, \quad (29)$$

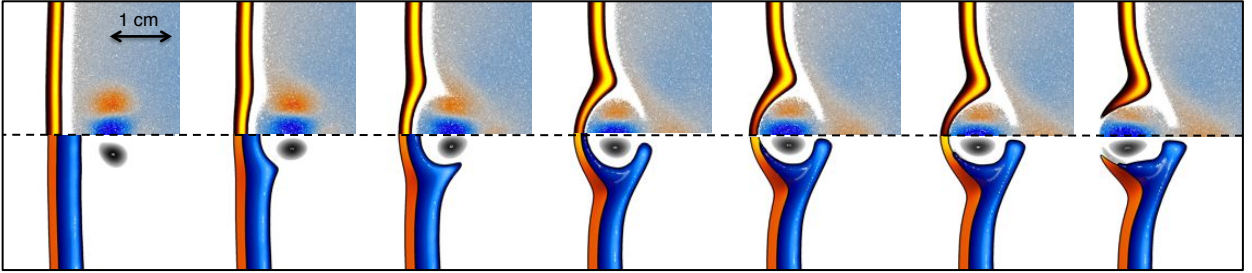
with  $T_b$  the boiling temperature. To determine the Spalding number, we evaluate all parameters using 0D calculations with a fixed gas temperature. Within the temperature range  $T \in [1500, 2400]$  K, the Spalding

number is almost linear with  $T$ , and  $B_M^0 \in [3.6, 6.7]$ . Therefore, depending on the chosen reference burnt gas temperature, the factor  $[\ln(1 + B_M^0)]^{-1}$  varies between 0.5 and 0.66. Consequently, the reference burnt gas temperature has a weak dependence on the evaporation time estimation, compared to the diameter variations considered in this study, which is a factor of two between each successive diameter, and therefore a factor four in terms of the evaporation time.

Choosing the reference temperature  $T = 2000$  K, for  $Sc = 0.7$ ,  $Sh = 2$ ,  $\mu = 4 \times 10^{-5} \text{ kg m}^{-1} \text{ s}^{-1}$  and  $\rho_l = 750 \text{ kg m}^{-3}$  the relationship between vaporization time and droplet diameter at injection is estimated as  $\tau_v = K d_0^2$  where  $K = 1.083 \times 10^6 \text{ s m}^{-2}$ .



(a) No extinction for case A. Instantaneous fields at normalized time  $\tau = 1.0, 2.0, 3.0, 3.5, 4.0, 4.5$ .



(b) Fuel depletion for case E. Instantaneous fields at normalized time  $\tau = 1.0, 2.0, 2.5, 2.9, 3.0, 3.1, 3.2$ .

Figure 17: Temporal evolution of the spray flame-vortex interaction when vortices are injected on the fuel side. Legend is the same as in Fig. 6. (For interpretation of the references to colour in this figure, the reader is referred to the web version of this article.)

### C. Effect of boundary conditions: pre-vaporized case

In our simulation, we have chosen a fixed mass loading at injection, as well as fixed temperature and velocities for gas and liquid phases. At this point, it could be of interest to evaluate the impact of these choices. First, the effect of mass loading at injection and velocities are characterized by the Damköhler number  $Da_r^e$ : it takes into account the injection velocity and mass loading through the strain rate at extinction for an unperturbed flame  $A_e$ . Second, concerning the effect of gas temperature, it also affects the chemical time scale, thus being taken into account in the Damköhler number too. Third, the liquid temperature and droplet diameters affect the evaporation time scale. If no pre-vaporization occurs, our diagram is expected to account for the effect of any choice of boundary conditions, as it will simply affect the vaporization time scale that only occurs in the flame. If pre-vaporization occurs, we do have to take into account an additional time scale:

$$\tau_{prev} = \frac{Sc \rho_l d_0^2}{4 Sh \mu \ln(B_M^{pre} + 1)}, \quad (30)$$

where  $B_M^{pre}$  is evaluated at the injection temperature. Then a vaporization Stokes number for pre-evaporation  $St_{prev} A_0 \tau_{prev}$  can be defined. If  $St_{prev} < 1$  the droplets are considered fully pre-vaporized, and the flame is a gaseous flame. If  $St_{prev} > 1$ , the droplets reach the flame. In this case, we have to evaluate the vaporization time scale in the flame using the diameter at the flame location  $d_f$ :

$$d_f^2 = \left(1 - \frac{1}{St_{prev}}\right) d_0^2. \quad (31)$$